Dynamics of Asymmetric and Symmetric Divisions of Muscle Stem Cells In Vivo and on Artificial Niches

Brendan Evano, Sara Khalilian, Gilles Le Carrou, Geneviève Almouzni, Shahragim Tajbakhsh

Cell Reports

Report

Dynamics of Asymmetric and Symmetric Divisions of Muscle Stem Cells *In Vivo* and on Artificial Niches

Graphical Abstract

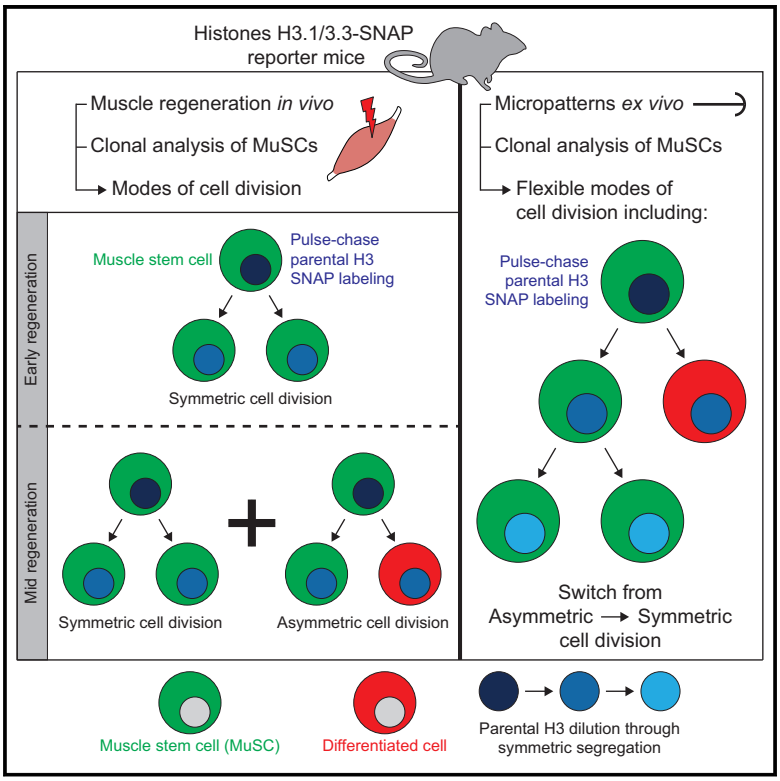

Highlights

- Muscle stem cells divide symmetrically and asymmetrically *in vivo*
- Muscle stem cells can switch from asymmetric to symmetric cell division *ex vivo*
- Histone H3-SNAP reporters allow turnover measurements *in vivo*
- H3.1 and H3.3 are symmetrically distributed during muscle stem cells divisions

Authors

Brendan Evano, Sara Khalilian, Gilles Le Carrou, Geneviève Almouzni, Shahragim Tajbakhsh

Correspondence

shahragim.tajbakhsh@pasteur.fr

In Brief

Using SNAP-tagged histone H3-reporter mice and clonogenic tracing, Evano et al. show that muscle stem cells can perform symmetric and asymmetric cell divisions (SCDs; ACDs) *in vivo*, and switch from ACDs to SCDs *ex vivo*, with symmetric inheritance of H3.1 and H3.3.

Evano et al., 2020, Cell Reports *30*, 3195–3206
March 10, 2020
https://doi.org/10.1016/j.celrep.2020.01.097

CellPress

Cell Reports
Report

Dynamics of Asymmetric and Symmetric Divisions of Muscle Stem Cells *In Vivo* and on Artificial Niches

Brendan Evano,[1,2,3] Sara Khalilian,[1,2,4] Gilles Le Carrou,[1,2,4] Geneviève Almouzni,[3] and Shahragim Tajbakhsh[1,2,5,*]
[1]Stem Cells and Development, Department of Developmental and Stem Cell Biology, Institut Pasteur, 25 Rue du Dr. Roux, 75015 Paris, France
[2]CNRS UMR 3738, Institut Pasteur, Paris 75015, France
[3]CNRS UMR 3664, Nuclear Dynamics, Institut Curie, Pavillon Pasteur, 26 Rue d'Ulm, 75005 Paris, France
[4]These authors contributed equally
[5]Lead Contact
*Correspondence: shahragim.tajbakhsh@pasteur.fr
https://doi.org/10.1016/j.celrep.2020.01.097

SUMMARY

Stem cells can be maintained through symmetric cell divisions (SCDs) and asymmetric cell divisions (ACDs). How and when these divisions occur *in vivo* in vertebrates is poorly understood. Here, we developed a clonogenic cell tracing method that demonstrates the asymmetric distribution of transcription factors along with old and new DNA in mouse muscle stem cells during skeletal muscle regeneration. Combining single-cell tracking and artificial niches *ex vivo*, we show how cells switch from ACDs to SCDs, suggesting that they are not engaged in an obligate mode of cell division. Further, we generated SNAP-tagged histone H3-reporter mice and find that, unlike fly germline stem cells, differential fate outcomes are associated with a symmetric distribution of the H3.1 and H3.3 histone variants in mouse muscle stem cells. This versatile and efficient H3-SNAP labeling system will allow an investigation of mechanisms underlying the maintenance of epigenomic identity and plasticity in a variety of tissues.

INTRODUCTION

In most tissues, stem cells self-renew and give rise to daughter cells committed to differentiation, thereby ensuring both tissue homeostasis and maintenance of the stem cell pool (Morrison and Kimble, 2006). This can be achieved through different modes of cell division, either symmetric cell divisions (SCDs)—self-renewing or differentiating—or asymmetric cell divisions (ACDs). Fine-tuning the balance between these different modes is critical for proper tissue development, homeostasis, and regeneration and for preventing tumorigenesis (Morrison and Kimble, 2006). In animal models, lineage tracing, proliferation assays, and statistical models have identified critical aspects of stem cell dynamics and fate determination in tissue development, homeostasis, and repair, as well as during tumor formation (Blanpain and Simons, 2013). Key questions in stem cell dynamics are whether individual cell lineages adopt fixed or variable modes of division over consecutive cell divisions, and to what extent homeostasis of the stem cell pool is orchestrated through invariant asymmetry or at the population level (Simons and Clevers, 2011). However, accessing this information in mammals has been limited by the few examples that are available for asymmetric fate decisions *in vivo* in mice with bona fide transcription factors as fate markers or analysis of consecutive cell divisions (Kim et al., 2015; Noctor et al., 2004).

A variety of subcellular constituents including transcripts, organelles, centrosomes, or sister chromatids can distribute asymmetrically between daughter cells during cell division (Knoblich, 2008; Venkei and Yamashita, 2018). A major challenge, though, is to understand how their biased segregation dictates or follows asymmetric cell fates (Evano and Tajbakhsh, 2013; Tajbakhsh and Gonzalez, 2009). The hypothesis of a role for replication-coupled nucleosome assembly in determining asymmetric cell fates in the *C. elegans* nervous system has raised much interest (Nakano et al., 2011). Furthermore, non-equivalent inheritance of specific histone variants during ACD of *D. melanogaster* male germline stem cells (GSCs) (Tran et al., 2012; Xie et al., 2015; Wooten et al., 2019), along with the implication of chromatin in cell plasticity (Yadav et al., 2018), raised the possibility of an epigenetic (i.e., chromatin modifications not affecting the primary DNA sequence) regulation of stem cell fate determination.

Adult muscle stem cells (MuSCs) are quiescent during homeostasis. Following muscle injury, they proliferate and reconstitute damaged muscle fibers, while a fraction of the population self-renews (Bentzinger et al., 2013; Evano and Tajbakhsh, 2018; Gayraud-Morel et al., 2009). This process is accompanied by a temporal expression of cell fate markers including the transcription factors Pax7 (stem), Myod (commitment), and Myogenin (differentiation). MuSCs can divide symmetrically and asymmetrically during muscle regeneration (Dumont et al., 2015a; Kuang et al., 2007; Lukjanenko et al., 2016; Rocheteau et al., 2012; Yennek et al., 2014). MuSCs reside in a specific niche where extrinsic and intrinsic cues assure MuSC proliferation and commitment (Dumont et al., 2015b; Evano and Tajbakhsh, 2018). As with other stem cell niches (Voog and Jones, 2010), the MuSC

Table 1. Comparison of Methods to Analyze Histone Dynamics

Method	Feature								References
-	Time Scale	Association Kinetics	Dissociation Kinetics	Histone Variants	Locus Specific	Genetic Perturbation	Required Small Molecules	Applicable In Vivo in Mouse	-
Pulse labeling (stable isotopes + mass spectrometry)	min to days	yes[a]	yes	yes	no	no	density labeled amino acids	not demonstrated	(Alabert et al., 2014; Xu et al., 2010)
Fluorescence measurements after photo bleaching/ switching	s to min	yes	yes[b]	yes	no	yes	no	not demonstrated	(Falk et al., 2015; Kimura and Cook, 2001; Liu et al., 2015)
Covalent attachment of tags to capture histones and identify turnover (CATCH-IT)	min to h	yes[a]	yes[c]	no	yes	no	azidohomoalanine (methionine substitute)	not demonstrated	(Deal et al., 2010)
Pulsed expression of tagged histones	h to days	yes[d]	yes	yes	yes	yes	inducers of gene expression	not demonstrated	(Ahmad and Henikoff, 2001, 2002; Dion et al., 2007; Huang et al., 2013; Katan-Khaykovich and Struhl, 2011; Mito et al., 2005; Tran et al., 2012)
SNAP-tags	min to h (fluorescent substrates)	yes[e]	yes[f]	yes	no	yes	benzylguanine-fluorophore	this study	reviewed in Siwek et al. (2018), this study
	h to days[g] (time-ChIP)	yes[e]	yes[f]	yes	yes	yes	benzylguanine-biotin	this study (not demonstrated)	

Adapted from Siwek et al. (2018) and updated.
[a]Dependent on protein translation rate
[b]When photo-switchable proteins are used
[c]Restricted to the recently incorporated histones
[d]Dependent on transcription and translation rates
[e]When combined with quench-chase-pulse assay
[f]When combined with pulse-chase assay
[g]Faster than pulsed expression of tagged histones

microenvironment is dynamic during muscle regeneration (Bentzinger et al., 2013), raising the possibility that some niche factors that cannot be modeled *ex vivo* might temporally regulate MuSC fate. Although ACDs have been reported extensively *ex vivo*, evidence for transcription factor and DNA asymmetry during ACD has been lacking for vertebrates *in vivo*.

Histone H3 variants have a major role in epigenetic maintenance during development and disease (Filipescu et al., 2014; Yadav et al., 2018), but tools to measure their turnover at the level of individual cells *in vivo* in whole organisms in vertebrates are still lacking. Thus, for these organisms, current knowledge on histone dynamics is restricted predominantly to *in vitro* models that do not fully account for niche-mediated influences. To address these questions and examine transcription factor asymmetry directly *in vivo*, we developed a pulse-chase approach to follow histone variants using SNAP-tags (Juillerat et al., 2003) and explored adult mouse skeletal MuSCs as a first model of changes in cell fate.

RESULTS

Establishment of H3.1-SNAP and H3.3-SNAP Reporter Mouse Lines

Histone dynamics has been addressed with a variety of approaches on bulk chromatin or at specific loci (Table 1). Although these methods provided significant insights into chromatin dynamics, many suffer from specific downsides in terms of positional information, time scale, amount of required material, or versatility. To examine histone H3 variant dynamics *in vivo*, we generated ubiquitous H3.1 and H3.3 reporters in mice using

SNAP-tags (see Method Details). *H3.1-SNAP* and *H3.3-SNAP* transgenes were expressed in all tested tissues, although with variable levels (Figure 1A) and at relatively low levels (<40%), compared to endogenous histones (Figure 1B). SNAP labeling of embryonic fibroblasts derived from reporter mice showed ubiquitous *H3.1-SNAP* expression, whereas *H3.3-SNAP* expression was lower (data not shown). We found that newly deposited H3.1-SNAP histones overlapped with sites of DNA synthesis, whereas newly deposited H3.3-SNAP histones were uncoupled from DNA synthesis (Figure 1C), as reported (Ray-Gallet et al., 2011). These results indicate that the *Tg:H3.1-SNAP* and *Tg:H3.3-SNAP* lines are faithful reporters of H3.1 and H3.3 turnover in mouse primary cells. In addition, incubation with a fluorescent SNAP substrate labeled MuSCs up to 60% *in vivo* (Figure 1D), although MuSCs represent a low fraction of total mononucleated muscle cells (<5%).

This high efficiency of SNAP labeling allowed us to investigate histone dynamics in mouse primary cells. As a proof of principle, we used MuSCs as a model to address whether the non-equivalent inheritance of specific histone H3 variants uncovered in *Drosophila* GSCs operates in a somatic mammalian stem cell.

MuSCs Perform Asymmetric Cell Fate Decisions and Non-random DNA Segregation *In Vivo*, Accompanied by Symmetric Segregation of Parental H3.1 Histones

To examine the modes of cell division and distribution of parental H3.1 histones in MuSCs *in vivo*, adult *Tibialis anterior* (TA) muscles were injured to induce the activation of MuSCs and muscle regeneration. We established a clonal tracing strategy (Cre-inducible membrane-GFP [mGFP]) to track sister cells in regenerating muscles *in vivo* (Figure 2A), together with SNAP labeling of parental H3.1 histones. If parental histones are partitioned equally following mitosis, the fluorescent SNAP signal will be inherited equally between daughter cells. However, if parental histones are inherited asymmetrically, the SNAP signal will be detected only in a subset of daughter cells (Figure 2B). We chose two time points for analysis: 3 days post-injury (dpi) where MuSCs undergo a transit-amplification phase; and 5 dpi, where MuSCs continue to proliferate, but differentiation and self-renewal to quiescence decisions are more frequent (Bentzinger et al., 2013; Joe et al., 2010; Rocheteau et al., 2012). At 5 dpi, we observed self-renewing (66.7%, n = 98/147 cell pairs; Figures 2C and 2D, left) and differentiating (6.8%, n = 10/147 cell pairs; Figures 2C and 2D middle-left) SCDs in addition to ACDs (23.1%, n = 34/147 cell pairs; Figures 2C and 2D, middle-right and right). Notably, the relative frequencies of the different modes of cell division observed *in vivo* at 5 dpi correspond to those obtained *ex vivo* with cells isolated from regenerating muscles at 5 dpi (Yennek et al., 2014). As in that previous study, we note that the frequency of SCDs might be overestimated at 5 dpi. At 3 dpi, we observed self-renewing (91.4%, n = 42/46 cell pairs; Figure S1A) and differentiating (4.3%, n = 2/46 cell pairs; Figure S1A) SCDs in addition to ACDs (4.3%, n = 2/46 cell pairs; Figure S1A). These results reveal a shift from self-renewing SCDs to ACDs during the early phases of muscle regeneration from 3 dpi to 5 dpi, consistent with exponential amplification of progenitors during the early phase of regeneration.

Independently of the modes of cell division, we observed an equivalent SNAP signal between daughter cells (Figure 2D), with an average difference of SNAP intensity between sister cells of 13.2% at 3 dpi (Figure S1B) and 19.3% at 5 dpi (Figure S1E). Analysis of the SNAP signal between sister cells after SCDs and ACDs showed similar patterns, indicative of a comparable histone distribution (Figures S1C and S1F). Altogether, these results are consistent with a symmetric inheritance of parental H3.1 histones during both SCDs and ACDs of MuSCs.

Our analysis also revealed a difference in SNAP signal intensity (2-3 fold) between daughter cells in a minor fraction of cell divisions at 3 and 5 dpi (≈5% of divisions; Figures 2D [left, right] and 2G [right]). Among all ACDs at 5 dpi, transcription factors showed a mean fold change in expression between sister cells of 3.7 for Pax7 (maximum 11.8) and 3.8 for Myogenin (maximum 9.2). Therefore, we classified these rare events as examples of random non-equivalence of SNAP signal, or a differential turnover of this variant between sister cells, rather than bona fide cases of asymmetric H3.1 distribution (Figure S1D).

The asymmetric distribution of old and new histones or nucleosome pools has been hypothesized as a possible epigenetic mechanism for non-random DNA segregation (NRDS) of old and new strands of DNA (Evano and Tajbakhsh, 2013, 2018; Lansdorp, 2007). The asymmetric segregation of stem (Pax7) and differentiation (Myogenin) transcription factors was previously shown to correlate in part with NRDS *ex vivo*, where old DNA strands are inherited by the stem cell and new DNA strands by the committed cell (Rocheteau et al., 2012; Yennek et al., 2014). However, robust *in vivo* evidence for NRDS is lacking, thereby limiting in-depth mechanistic studies. To examine parental H3.1 histone distribution and NRDS *in vivo*, we adopted the same strategy as above, together with a 5-ethynyl-2′-deoxyuridine (EdU) pulse-chase labeling (Figures 2A and 2E) to identify old DNA strands (EdU pulse) and new DNA strands (EdU chase). We observed clonal examples of random DNA segregation (23.1%, n = 12/52 cell pairs; Figures 2F and 2G, left) and NRDS (76.9%, n = 40/52 cell pairs; Figures 2F [middle] and 2G [middle and right]). Interestingly, 22.5% of the cell pairs with NRDS showed asymmetric Myogenin expression (n = 9/40 NRDS cell pairs; Figures 2F and 2G, right), with Myogenin being expressed in the EdU-negative cell, as reported previously *ex vivo*, where parental DNA strands are labeled and inherited by the Pax7-expressing cell (Rocheteau et al., 2012; Yennek et al., 2014). Independently of the modes of DNA segregation, we observed an equivalent SNAP signal between daughter cells (Figure 2G, left and middle), with an average difference in SNAP intensity between sister cells of 18.2% (Figure S1G, left). As with our analysis of cell fate decisions (Figure 2D), we observed rare examples of non-equivalent SNAP signal between daughter cells (Figure 2G, right), and NRDS events were generally associated with symmetric SNAP signal between daughter cells (Figure S1G, right). Our results reveal a symmetric parental H3.1 inheritance, independent of the mode of DNA segregation detected by our method.

Parental H3.1 and H3.3 Histones Are Symmetrically Distributed during Asymmetric Cell Fate Decisions *Ex Vivo*

Because of the extensive migration of MuSCs during muscle regeneration (Webster et al., 2016), the *in vivo* lineage-tracing strategy we established did not allow tracking cells over multiple

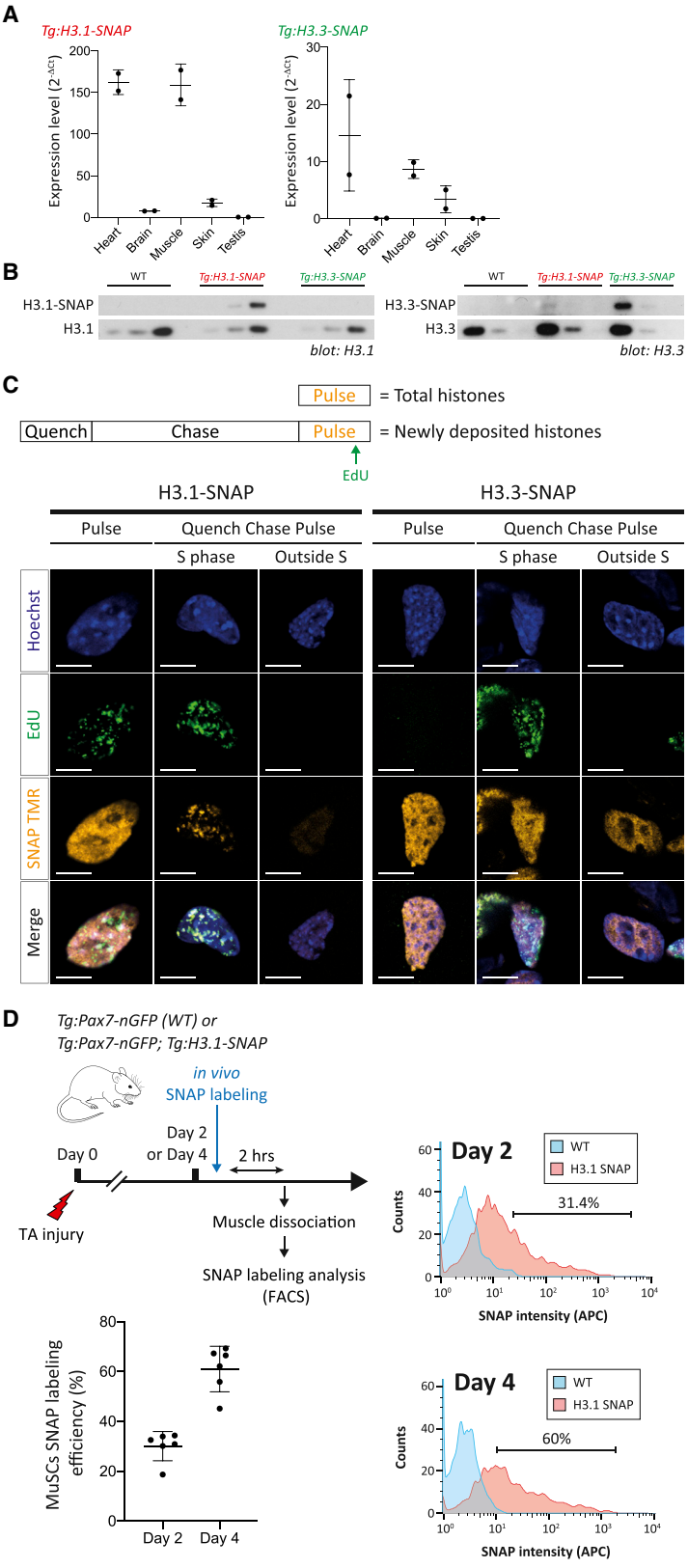

Figure 1. *Tg:H3.1-SNAP* and *Tg:H3.3-SNAP* Reporter Lines and *In Vivo* SNAP Labeling of MuSCs

(A) Transgene expression level (qRT-PCR) from heart, brain, skeletal muscle, skin, and testis; n = 2 mice per genotype. Data are presented as mean ± SD.

(B) Transgene expression level (western blot) from primary embryonic fibroblasts derived from wild-type (WT), *Tg:H3.1-SNAP*, and *Tg:H3.3-SNAP* mice, detected with anti-H3.1 (left) or anti-H3.3 (right) antibodies. Each panel shows the endogenous (bottom) and SNAP-tagged (top) histone variant. Different amounts of material loaded, centered on 1 μg over a range of 2-3-fold loading. n = 3 experiments.

(C) SNAP TMR labeling of total (pulse) or newly deposited (quench-chase pulse) SNAP-tagged histone variants and DNA replication sites (EdU) in *Tg:H3.1-SNAP* and *Tg:H3.3-SNAP* primary fibroblasts. Scale bar, 10 μm. n = 2 experiments.

(D) Efficiency of *in vivo* SNAP labeling of MuSCs at 2 and 4 days post-injury (dpi). In total, 30% or 60% of *Tg:H3.1-SNAP* MuSCs were labeled compared to WT control cells at 2 and 4 dpi, respectively; n = 6 transgenic mice for each time point. Data are presented as mean ± SD. Fluorescence-activated cell sorting (FACS) histograms indicate representative examples of SNAP labeling efficiency of MuSCs at 2 and 4 dpi.

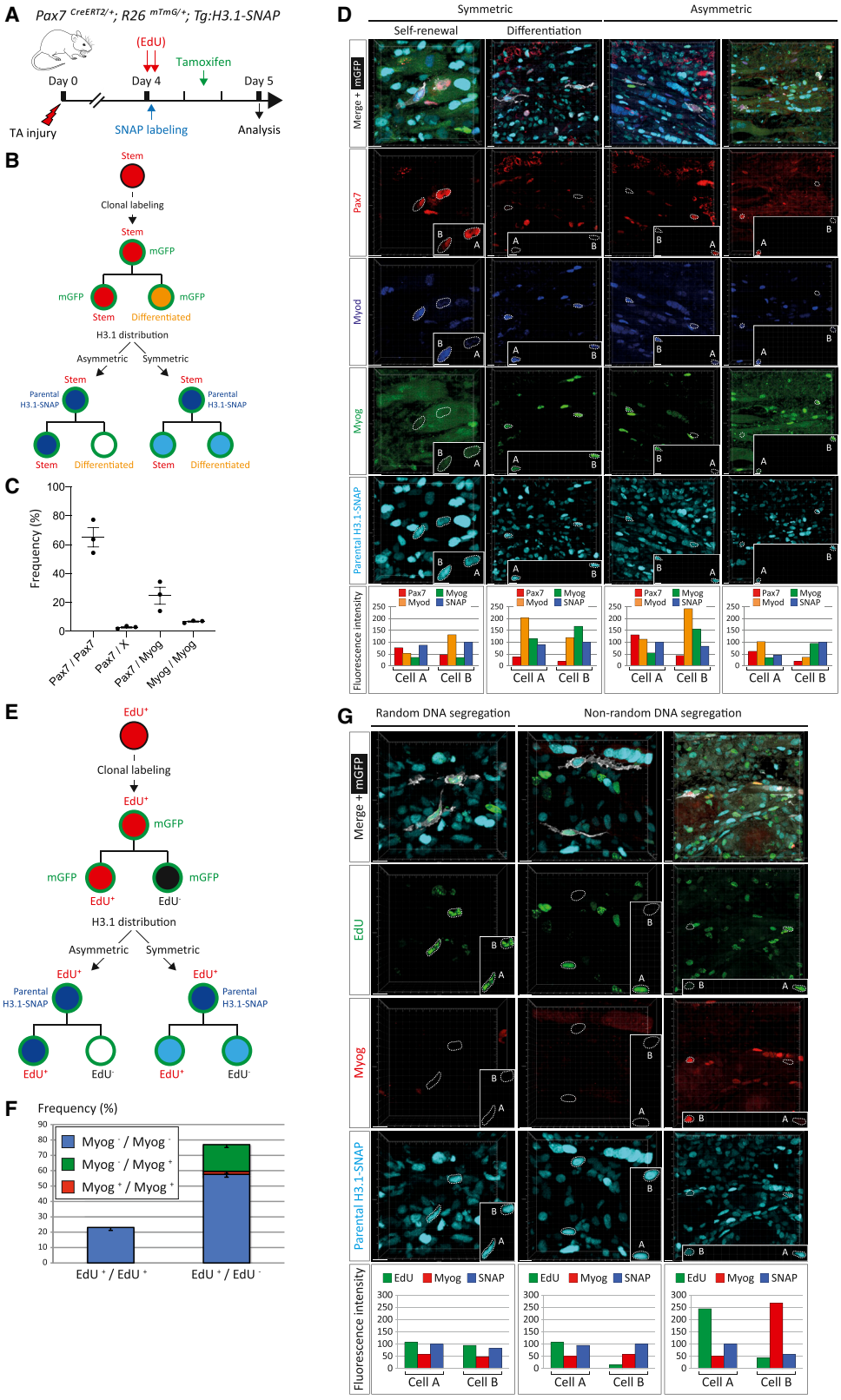

(legend on next page)

divisions with confidence. Therefore, we developed an *ex vivo* assay (Figure 3A; Method Details) on micropatterns to track histone distribution after one or two divisions (Figures 3 and 4). Micropatterns provide a controlled microenvironment that allows the confinement of single cells and their progeny (Videos S1, S2, and S3) (Théry et al., 2005). We and others have shown that their geometry impacts the frequency of ACD of stem cells (Freida et al., 2013; Yennek et al., 2014). After one division on micropatterns (Video S1), we observed self-renewing (Figures 3B [left] and 3D [left]) and differentiating (Figures 3B [middle] and 3D [middle]) SCDs in addition to ACDs (Figures 3B [right] and 3D [right]). The relative frequencies of the modes of cell division were similar for H3.1-SNAP (Figure 3C) and H3.3-SNAP cells (Figure 3E).

In all cases, SNAP-labeled H3.1 and H3.3 were distributed equivalently between daughter cells (Figures 3C and 3E), with average differences in SNAP intensity between sister cells of 11% and 11.7%, respectively. As with our *in vivo* analyses (Figure 2), we observed rare examples of non-equivalent SNAP intensity between daughter cells up to 1.4-fold, while the ACD of transcription factors showed a mean fold change of 4.9 for Pax7 (maximum 14.6) and 8.4 for Myogenin (maximum 23.0) expression. In agreement with our observations, we examined MuSCs on micropatterns after *in vivo* amplification and observed that parental H3.1 histones were essentially inherited symmetrically (Figures S3A–S3C). H3-Thr3 phosphorylation ($H3T3^P$) was reported to distinguish pre-existing and newly deposited H3 in prophase and to be required for asymmetric inheritance of old versus new histones in *D. melanogaster* GSCs (Xie et al., 2015). To further address the issue of histone inheritance, we investigated the distribution of $H3T3^P$ in *in vivo* activated/SNAP-labeled MuSCs on micropatterns. We readily detected $H3T3^P$ signals in mitotic cells, colocalizing with SNAP signals, yet not restricted to a subset of chromatids in early mitosis. These observations indicate that $H3T3^P$ did not point to a differential distribution of old versus new histones in early mitosis of MuSCs (Figure S3D), thereby confirming results obtained using H3.1-SNAP labeled histones. Therefore, these results indicate that parental H3.1 and H3.3 histones were essentially inherited symmetrically *ex vivo* during both SCD and ACD of MuSCs.

MuSCs Can Switch from ACDs to SCDs *Ex Vivo*

We next wondered whether parental histones could be asymmetrically distributed in the division that precedes the asymmetric expression of cell fate markers. MuSCs can divide multiple times on micropatterns, giving rise to clusters of cells. For example, the division of a mother cell can be followed by the division of one or both daughter cells, a process that we tracked using the notion that SNAP-histones distributed symmetrically during MuSC division. Notably, within each cluster of three cells, we observed two cells with, on average, half the SNAP intensity of the third cell (for both H3.1-SNAP and H3.3-SNAP; Figures 4A and 4D–4G), indicating a progressive dilution of parental histones by symmetric segregation over two consecutive divisions, irrespective of the modes of division at the first or second division.

We observed the following clusters of 3 cells: 3 $Pax7^+$; 2 $Pax7^+$ and 1 $Myog^+$; 1 $Pax7^+$ and 2 $Myog^+$; and 3 $Myog^+$ (Figure 4A). Given that Myog-expressing cells are post-mitotic (Andrés and Walsh, 1996; Zhang et al., 1999), we sought to determine the combinations of consecutive SCDs or ACDs that yield such clusters (Figures 4D–4G). Based on the observed frequencies of the different modes of cell division (Figure 3) and assuming that the first and second divisions follow the same ratios, we calculated (see Method Details) the expected frequency of each type of cluster (Figure 4B, top panel). Although clusters with three $Myog^+$ cells were at the expected frequency, clusters with 1 $Pax7^+$ and 2 $Myog^+$ cells were under-represented, and clusters with 3 $Pax7^+$ cells or 2 $Pax7^+$ and 1 $Myog^+$ cells were over-represented (Figure 4B, bottom panel).

Given that the modes of division in Figures 4D and 4F had predictable outcomes, we sought to establish the frequency of events depicted in Figures 4E and 4G, which can arise from two possible scenarios. Because of the dense confinement of cells and their rapid movements on micropatterns, it was difficult to track each cell with confidence over two consecutive divisions (Video S2). Therefore, we exploited symmetric SNAP dilution to reconstruct their proliferative hierarchy retrospectively: the cell with high SNAP was generated after the first cell division, while

Figure 2. MuSCs Perform Asymmetric Cell Fate Decisions and Non-random DNA Segregation *In Vivo*, Accompanied by Symmetric Segregation of Parental H3.1 Histones

(A) Experimental scheme. Lineage tracing was tamoxifen induced 14 h before analysis; parental histones were labeled 8 h before tamoxifen administration; old DNA strands were labeled with EdU (E–G) 9 and 7 h before tamoxifen administration.

(B) Potential parental histone distribution patterns during asymmetric cell fate decisions.

(C) Frequencies of different modes of cell division. Rare examples of Pax7/X and Myog/X daughter cells were observed, where one daughter cell expresses Pax7 or Myog and the other neither Pax7 nor Myog. n = 3 mice, n = 147 divisions. Data are presented as mean ± SEM.

(D) Representative examples of parental H3.1 inheritance pattern during self-renewing (left) or differentiating (middle-left) SCDs or ACDs (middle-right and right). mGFP signal from labeled daughter cells is shown only in the merged image for clarity; nuclei of daughter cells are outlined. Insets show nuclei of daughter cells isolated from other cells. Bottom panels indicate normalized fluorescence intensity of Pax7, Myod, Myog, and H3.1-SNAP for each example (see Method Details). Due to the regulation of MyoD during cell cycle progression (Lahmann et al., 2019), MyoD expression pattern was omitted from our analyses of modes of cell division. See Figure S2A for corresponding low-magnification images showing clonality. Scale bar, 10 μm.

(E) Potential parental histone distribution patterns during NRDS.

(F) Frequencies of the different modes of DNA segregation (random EdU^+/EdU^+ and non-random EdU^+/EdU^-) and fate decisions assessed by Myogenin expression. n = 2 mice, n = 52 divisions. Data are presented as mean ± SEM.

(G) Representative examples of parental H3.1 inheritance pattern during random DNA segregation (left) or NRDS (middle and right), with symmetric absence of Myogenin expression (left and middle) or asymmetric Myogenin expression (right). mGFP signal from labeled daughter cells is shown only in merged image for clarity; nuclei of daughter cells are outlined. Insets show nuclei of daughter cells isolated from other cells. Bottom panels indicate normalized fluorescence intensity of Myog, EdU, and H3.1-SNAP for each example (see Method Details). See Figure S2B for corresponding low-magnification images showing clonality. Scale bar, 10 μm.

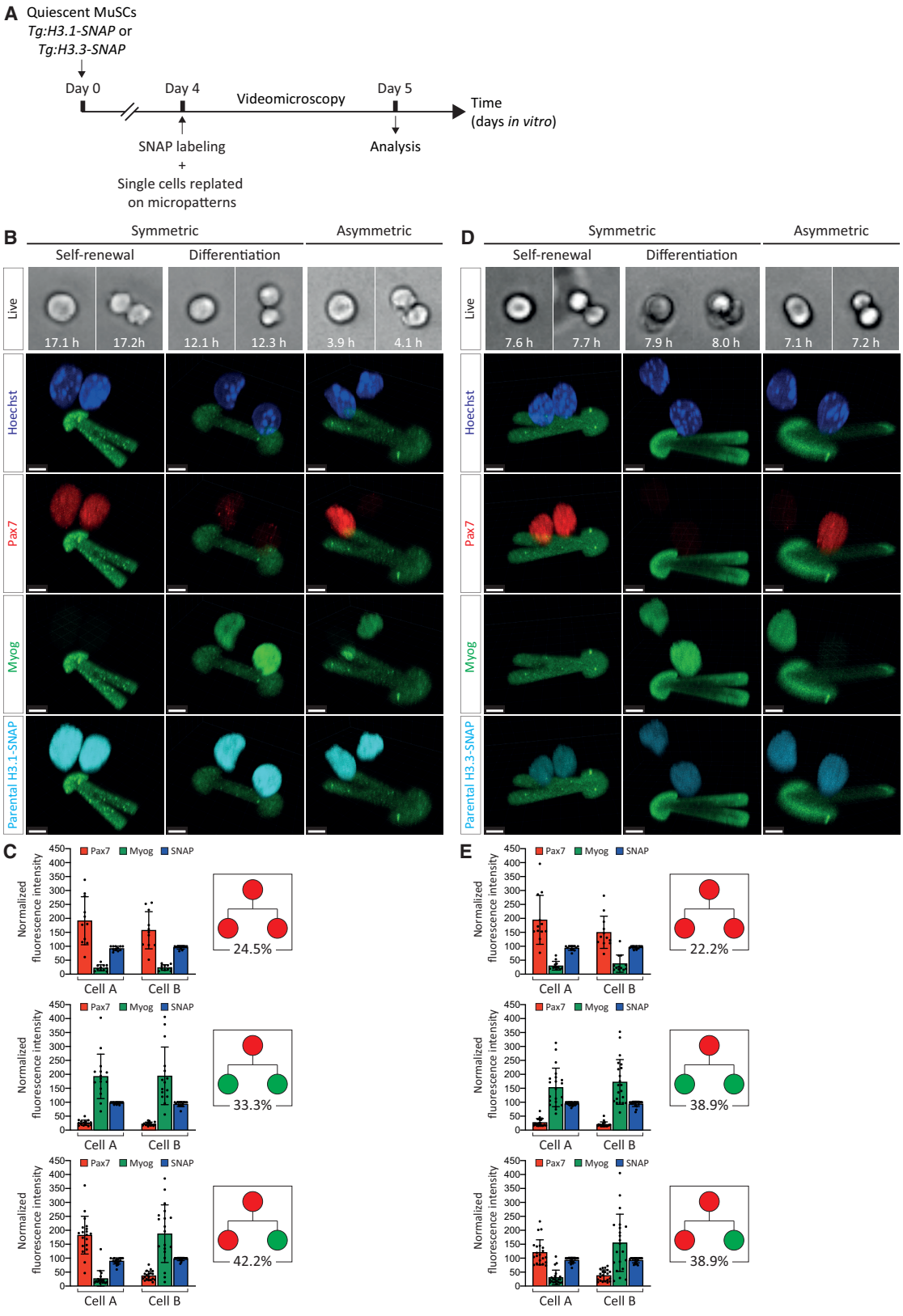

(legend on next page)

the two cells with lower SNAP intensity were generated after the second cell division (Figure 4C). Within clusters with 2 Pax7$^+$ and 1 Myog$^+$ cells, we noted that the Myog$^+$ cell always displayed the highest SNAP intensity (Figures 4A [example 2] and 4E), indicating that it was generated after the first cell division. Hence, such clusters derive from an initial ACD followed by a self-renewing SCD; the alternative scenario (self-renewing SCD followed by ACD) was not observed (Figure 4E). We noted only two examples of clusters with 1 Pax7$^+$ and 2 Myog$^+$ cells: one deriving from two consecutive ACDs (Figure 4A, example 3) and one deriving from a self-renewing SCD followed by a differentiating SCD, as inferred from the SNAP dilution patterns (Figure 4G; total n = 39).

We then calculated the frequencies of the different modes of cell division specifically for the second division and observed a striking loss in ACDs and a corresponding increase in self-renewing SCDs (Figure 4I), compared to the ratios observed for the first division (Figure 4H). This indicated that cells did not engage in obligate modes of cell division but could switch modes during consecutive divisions. Interestingly, an initial ACD was almost always followed by a SCD on micropatterns (n = 26/27). We hypothesize that the absence of ACDs at the second division could result from a counting mechanism or from a neighbor effect. However, the presence of an unrelated cell did not prevent the execution of ACDs in three-cell clusters (Figure S4). Furthermore, by tracking sequential mitoses, we provide further support for the symmetric distribution of the histone variants to daughter cells.

DISCUSSION

MuSC self-renewal has been extensively studied *ex vivo*, using mostly the first activation division on single myofiber explants (Le Grand et al., 2009; Kuang et al., 2007; Troy et al., 2012) or isolated MuSCs (Conboy et al., 2007; Liu et al., 2012; Rocheteau et al., 2012; Yennek et al., 2014). Here, we report an *ex vivo* assay with a high frequency of MuSC ACDs, using live imaging to ensure the clonality of the analyzed events and histone dilution to reconstruct the proliferative hierarchies retrospectively after consecutive cell divisions. Our results show that MuSCs can alternate between SCDs and ACDs. These findings suggest that an intrinsic counting mechanism, or extrinsic communication through interactions between sister cells, might regulate this switch. Interestingly, Notch signaling between sister myogenic cells was proposed to mediate asymmetric cell fates (Kuang et al., 2007). However, our results lead us to exclude the existence of a simple neighbor effect controlling this switch (Figure S4). Alternatively, cytokinesis remnants such as the midbody have been recently proposed to be asymmetrically inherited between cells and to serve as signaling platforms controlling stem cell proliferation and fate (Crowell et al., 2014; Dionne et al., 2015).

A recent study on muscle regeneration identified time windows of MuSC self-renewal and differentiation (Pawlikowski et al., 2019). To date, direct measurement of MuSC modes of cell division *in vivo* with single-cell resolution is lacking. Our findings show unambiguously that asymmetric cell fate decisions, with defined stem cell and differentiated cell transcription factors, take place during MuSC divisions and that this event correlates with NRDS directly *in vivo*. In addition, our analyses show that MuSCs perform mostly self-renewing SCDs at 3 dpi, while they can execute SCDs and ACDs at 5 dpi. These observations indicate that MuSCs can switch from SCDs to ACDs *in vivo* between 3 and 5 dpi, and this correlates with a decrease in their proliferative potential (Joe et al., 2010; Pawlikowski et al., 2019). Our complementary *ex vivo* studies tracking single cells over consecutive cell divisions revealed an unexpected switch from ACD to SCD. Systematic analysis of consecutive modes of cell divisions *in vivo* during muscle regeneration will be required to fully understand the dynamics of the stem cell population and whether some cells adopt invariant or stochastic modes of cell division. In addition, we restricted our analysis of modes of cell division to Pax7 and Myogenin distribution patterns. However, our results also identified asymmetric Myod distribution which we did not consider in the analysis due to its cell cycle regulation (Lahmann et al., 2019). If this expression pattern, combined with that of other fate markers, can be verified in future studies, we anticipate that the frequency of ACDs would increase accordingly.

A long-standing question in multicellular organisms is how epigenetic information is transmitted or altered through cell division. It is therefore critical to determine how, and where in the genome, the choice of histone variants, their turnover, and the post-translational modifications contribute to the maintenance or switch of a particular cell fate in primary cells in their *in vivo* environment. The ideal tool to measure histone dynamics would allow the *in vivo* analysis of fast and long-term association and dissociation kinetics of histone variants, with locus-specific information, without genetic perturbation through forced expression of tagged histones, and without requiring incubation with small molecules. SNAP-tagged histones provide a robust and versatile, complementary approach to existing strategies to measure histone dynamics (Table 1), notably with the recent advent of time-chromatin immunoprecipitation (ChIP) (Deaton et al., 2016; Siwek et al., 2018). The H3.1/3.3-SNAP mice we

Figure 3. Parental H3.1 and H3.3 Histones Are Symmetrically Distributed during Asymmetric Cell Fate Decisions *Ex Vivo*

(A) Experimental scheme (see Method Details).

(B) Representative examples of parental H3.1 inheritance pattern during self-renewing (left) and differentiating (middle) SCDs and ACDs (right). Scale bar, 5 μm. Cells were monitored by videomicroscopy to ensure the clonality of the analyzed events (time: hours post-plating on micropatterns).

(C) Mean normalized fluorescence intensity (see Method Details) of Pax7, Myogenin, and H3.1-SNAP during self-renewing SCDs (top panel, 24.5%), differentiating SCDs (middle panel, 33.3%), and ACDs (bottom panel, 42.2%); n = 2 experiments. n = 45 cell pairs. Data are presented as mean ± SD.

(D) Representative examples of parental H3.3 inheritance pattern during self-renewing (left) and differentiating (middle) SCDs and ACDs (right). Scale bar, 5 μm. Cells were monitored by videomicroscopy to ensure the clonality of the analyzed events (time: hours post-plating on micropatterns).

(E) Mean normalized fluorescence intensity (see Method Details) of Pax7, Myogenin, and H3.3-SNAP during self-renewing SCDs (top panel, 22.2%), differentiating SCDs (middle panel, 38.9%), and ACDs (bottom panel, 38.9%); n = 2 experiments. n = 54 cell pairs. Data are presented as mean ± SD.

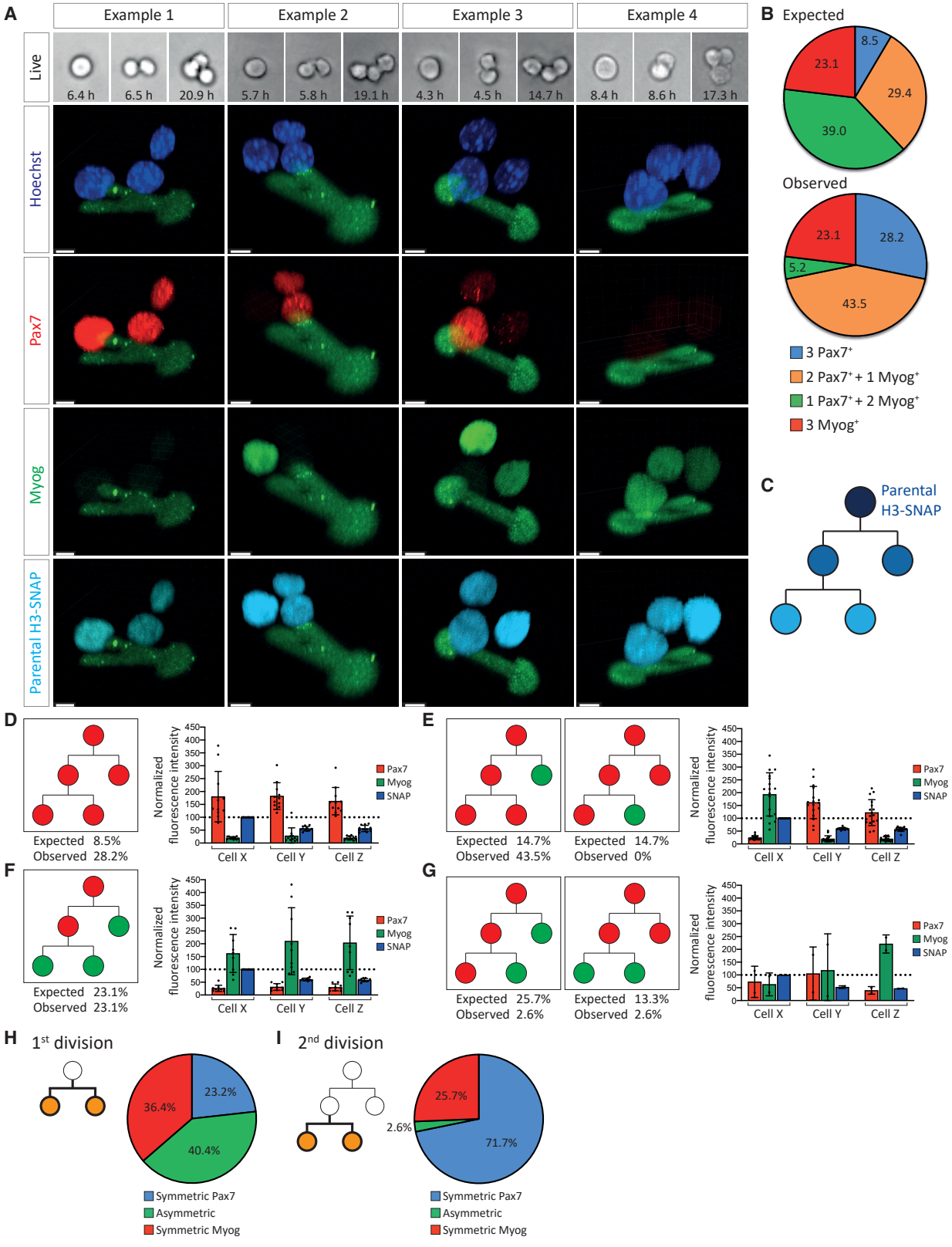

(legend on next page)

generated will allow investigating mechanisms of epigenetic identity, plasticity, and dynamics in a variety of cell types in their *in vivo* environment.

The high efficiency of *in vivo* SNAP pulse-chase labeling allowed us to address the inheritance pattern of parental H3.1/3.3 histones in dividing mouse MuSCs and to track consecutive cell divisions. We conclude here that asymmetric cell fate decisions and NRDS are not necessarily driven by a global asymmetric inheritance of old and new pools of H3.1. This finding contrasts with the case of stem cells in *D. melanogaster* male germline (Tran et al., 2012; Xie et al., 2015), where asymmetric histone distribution has been shown to result from the retention of parental histones on the leading strand and preferential unidirectional DNA replication (Wooten et al., 2019). While our results address the global inheritance of parental histones and cannot exclude local limited asymmetry, notably at the replication fork, more comparative work will be required to determine whether the difference observed between *D. melanogaster* GSCs and mouse MuSCs reflects differences in the reporters used, lack of conservation through evolution of the molecular mechanisms of asymmetric histone inheritance, or mechanistic differences between GSCs and somatic stem cells. More generally, future detailed studies using the protocols and H3-SNAP reporters we established should allow further assessment of histone, transcription factor, and DNA segregation dynamics in multiple tissues during growth, regeneration, and aging.

STAR★METHODS

Detailed methods are provided in the online version of this paper and include the following:

- KEY RESOURCES TABLE
- LEAD CONTACT AND MATERIALS AVAILABILITY
- EXPERIMENTAL MODEL AND SUBJECT DETAILS
  - Mouse strains
  - Cell lines and culture conditions
- METHOD DETAILS
  - Establishment of H3.1/H3.3-SNAP mouse strains
  - qRT-PCR
  - Western blot
  - SNAP labeling
  - Muscle injury, tamoxifen and EdU delivery
  - MuSCs isolation
  - *Ex vivo* modes of cell division
  - Micropatterns
  - Live-imaging
  - Immunocytochemistry and Immunohistochemistry
  - Antibody fluorescent labeling
  - Image analysis and quantification
  - Analysis of parental histone distribution
  - Analysis of modes of cell division
- QUANTIFICATION AND STATISTICAL ANALYSIS
- DATA AND CODE AVAILABILITY

SUPPLEMENTAL INFORMATION

Supplemental Information can be found online at https://doi.org/10.1016/j.celrep.2020.01.097.

ACKNOWLEDGMENTS

This work was supported by Institut Pasteur and grants from Agence Nationale de la Recherche ANR, (Laboratoire d'Excellence Revive, Investissement d'Avenir; ANR-10-LABX-73, ANR-16-CE12-0024) and Association Française contre les Myopathies, AFM, le Centre national de la recherche scientifique Centre national de la recherche scientifique, (CNRS), and the European Research Council (Advanced Research Grant 332893). We thank the Mouse Genetics Engineering Platform (Institut Pasteur), the Flow Cytometry and Photonic Bioimaging Platforms of the Center for Technological Resources and Research (Institut Pasteur),and J. van der Vlag (Radboud University, Netherlands) for providing H3.1 antibody; T. Cheung (Hong Kong University of Science and Technology) for advice on antibody labelling; B. Vianay (Cytomorpholab, Hôpital Saint-Louis, Paris) for advice on micropatterning; and Tajbakhsh and Almouzni lab members for advice on SNAP labelling. G.A. received support from the French National Research Agency (ANR),

Figure 4. MuSCs Can Switch from ACDs to SCDs *Ex Vivo*

(A) Representative examples of clusters with three cells arising from a single cell. Cells were monitored by videomicroscopy to ensure the clonality of the analyzed events (time: hours post-plating on micropatterns). Clusters with 3 $Pax7^+$ cells (example 1) can arise from two consecutive self-renewing SCDs (D); clusters with 2 $Pax7^+$ and 1 $Myog^+$ cells (example 2) can arise from a first ACD followed by a self-renewing SCD or from a first self-renewing SCD followed by an ACD (E); clusters with 1 $Pax7^+$ and 2 $Myog^+$ cells (example 3) can arise from two consecutive ACDs or a first self-renewing SCD followed by differentiating SCD (G); and clusters with 3 $Myog^+$ cells (example 4) can arise from a first ACD followed by a differentiating SCD (F). Scale bar, 5 μm.

(B) Expected and observed frequencies of the different clusters of three cells.

(C) Strategy to reconstruct the proliferative hierarchy of clusters of three cells retrospectively using SNAP dilution. As MuSCs expressing H3.1-SNAP or H3.3-SNAP displayed similar histone segregation patterns and modes of cell division (Figure 3), clusters of three cells deriving from *Tg:H3.1-SNAP* or *Tg:H3.3-SNAP* MuSCs were pooled for analyses (D–I) (see also Figure S4).

(D–G) Mean normalized fluorescence intensity (see Method Details) of Pax7, Myogenin, and H3-SNAP of the four scenarios in three-cell clusters with expected and observed frequencies; n = 2 experiments, n = 39 clusters. Data are presented as mean ± SD. Expected frequencies were calculated knowing that $Myog^+$ cells are post-mitotic and assuming that the first and second divisions follow the same ratios. Clusters of three cells were first classified according to the four different types observed. In addition, cells within each cluster of three cells were ranked with decreasing normalized SNAP intensity and named "Cell X," "Cell Y," and "Cell Z."

(D) Clusters with 3 $Pax7^+$ cells; n = 11 clusters.

(E) Clusters with 2 $Pax7^+$ and 1 $Myog^+$ cells. n = 17 clusters. Observed frequency of each scenario by assigning each observed cluster based on SNAP intensity of $Myog^+$ cell (high-SNAP $Myog^+$ cell, generated at first division; low -SNAP $Myog^+$ cell, generated at second division).

(F) Clusters with 3 $Myog^+$ cells; n = 9 clusters.

(G) Clusters with 1 $Pax7^+$ and 2 $Myog^+$ cells; n = 2 clusters. Observed frequency was calculated by assigning each observed cluster based on SNAP intensity of $Pax7^+$ cell (high-SNAP $Pax7^+$ cell, generated at first division; low-SNAP $Pax7^+$ cell, generated at second division).

(H) Observed frequencies of modes of cell division at first division (pooled H3.1-SNAP and H3.3-SNAP cell pairs from Figure 3).

(I) Observed frequencies of modes of cell division at second division (see Method Details).

Investissement D'avenir Labex développement, épigenèse, épigénétique et potentiel (DEEP), and the European Research Council Advanced (grant ChromAdict).

AUTHOR CONTRIBUTIONS

B.E. and S.T. proposed the concept, designed experiments, and wrote the paper. B.E. performed and analyzed the experiments. S.K. and G.L.C. provided technical support. G.A. contributed to the proposal preparation for funding of the project, advised on experiments and interpretation along with her team, and edited the paper. All authors read and agreed on the manuscript.

DECLARATION OF INTERESTS

The authors declare no competing interests.

Received: April 9, 2019
Revised: November 26, 2019
Accepted: January 28, 2020
Published: March 10, 2020

REFERENCES

Adam, S., Polo, S.E., and Almouzni, G. (2013). Transcription recovery after DNA damage requires chromatin priming by the H3.3 histone chaperone HIRA. Cell *155*, 94–106.

Ahmad, K., and Henikoff, S. (2001). Centromeres are specialized replication domains in heterochromatin. J. Cell Biol. *153*, 101–110.

Ahmad, K., and Henikoff, S. (2002). The histone variant H3.3 marks active chromatin by replication-independent nucleosome assembly. Mol. Cell *9*, 1191–1200.

Alabert, C., Bukowski-Wills, J.-C., Lee, S.-B., Kustatscher, G., Nakamura, K., de Lima Alves, F., Menard, P., Mejlvang, J., Rappsilber, J., and Groth, A. (2014). Nascent chromatin capture proteomics determines chromatin dynamics during DNA replication and identifies unknown fork components. Nat. Cell Biol. *16*, 281–293.

Andrés, V., and Walsh, K. (1996). Myogenin expression, cell cycle withdrawal, and phenotypic differentiation are temporally separable events that precede cell fusion upon myogenesis. J. Cell Biol. *132*, 657–666.

Bentzinger, C.F., Wang, Y.X., Dumont, N.A., and Rudnicki, M.A. (2013). Cellular dynamics in the muscle satellite cell niche. EMBO Rep. *14*, 1062–1072.

Blanpain, C., and Simons, B.D. (2013). Unravelling stem cell dynamics by lineage tracing. Nat. Rev. Mol. Cell Biol. *14*, 489–502.

Bodor, D.L., Valente, L.P., Mata, J.F., Black, B.E., and Jansen, L.E.T. (2013). Assembly in G1 phase and long-term stability are unique intrinsic features of CENP-A nucleosomes. Mol. Biol. Cell *24*, 923–932.

Clément, C., Orsi, G.A., Gatto, A., Boyarchuk, E., Forest, A., Hajj, B., Miné-Hattab, J., Garnier, M., Gurard-Levin, Z.A., Quivy, J.-P., and Almouzni, G. (2018). High-resolution visualization of H3 variants during replication reveals their controlled recycling. Nat. Commun. *9*, 3181.

Conboy, M.J., Karasov, A.O., and Rando, T.A. (2007). High incidence of non-random template strand segregation and asymmetric fate determination in dividing stem cells and their progeny. PLoS Biol. *5*, e102.

Crowell, E.F., Gaffuri, A.-L., Gayraud-Morel, B., Tajbakhsh, S., and Echard, A. (2014). Engulfment of the midbody remnant after cytokinesis in mammalian cells. J. Cell Sci. *127*, 3840–3851.

Deal, R.B., Henikoff, J.G., and Henikoff, S. (2010). Genome-wide kinetics of nucleosome turnover determined by metabolic labeling of histones. Science *328*, 1161–1164.

Deaton, A.M., Gómez-Rodríguez, M., Mieczkowski, J., Tolstorukov, M.Y., Kundu, S., Sadreyev, R.I., Jansen, L.E., and Kingston, R.E. (2016). Enhancer regions show high histone H3.3 turnover that changes during differentiation. eLife *5*, e15316.

Dion, M.F., Kaplan, T., Kim, M., Buratowski, S., Friedman, N., and Rando, O.J. (2007). Dynamics of replication-independent histone turnover in budding yeast. Science *315*, 1405–1408.

Dionne, L.K., Wang, X.-J., and Prekeris, R. (2015). Midbody: from cellular junk to regulator of cell polarity and cell fate. Curr. Opin. Cell Biol. *35*, 51–58.

Dumont, N.A., Wang, Y.X., von Maltzahn, J., Pasut, A., Bentzinger, C.F., Brun, C.E., and Rudnicki, M.A. (2015a). Dystrophin expression in muscle stem cells regulates their polarity and asymmetric division. Nat. Med. *21*, 1455–1463.

Dumont, N.A., Wang, Y.X., and Rudnicki, M.A. (2015b). Intrinsic and extrinsic mechanisms regulating satellite cell function. Development *142*, 1572–1581.

Evano, B., and Tajbakhsh, S. (2013). Sorting DNA with asymmetry: a new player in gene regulation? Chromosome Res. *21*, 225–242.

Evano, B., and Tajbakhsh, S. (2018). Skeletal muscle stem cells in comfort and stress. NPJ Regen. Med. *3*, 24.

Falk, S.J., Guo, L.Y., Sekulic, N., Smoak, E.M., Mani, T., Logsdon, G.A., Gupta, K., Jansen, L.E.T., Van Duyne, G.D., Vinogradov, S.A., et al. (2015). Chromosomes. CENP-C reshapes and stabilizes CENP-A nucleosomes at the centromere. Science *348*, 699–703.

Filipescu, D., Müller, S., and Almouzni, G. (2014). Histone H3 variants and their chaperones during development and disease: contributing to epigenetic control. Annu. Rev. Cell Dev. Biol. *30*, 615–646.

Freida, D., Lecourt, S., Cras, A., Vanneaux, V., Letort, G., Gidrol, X., Guyon, L., Larghero, J., and Thery, M. (2013). Human bone marrow mesenchymal stem cells regulate biased DNA segregation in response to cell adhesion asymmetry. Cell Rep. *5*, 601–610.

Gayraud-Morel, B., Chrétien, F., Flamant, P., Gomès, D., Zammit, P.S., and Tajbakhsh, S. (2007). A role for the myogenic determination gene Myf5 in adult regenerative myogenesis. Dev. Biol. *312*, 13–28.

Gayraud-Morel, B., Chrétien, F., and Tajbakhsh, S. (2009). Skeletal muscle as a paradigm for regenerative biology and medicine. Regen. Med. *4*, 293–319.

Hinner, M.J., and Johnsson, K. (2010). How to obtain labeled proteins and what to do with them. Curr. Opin. Biotechnol. *21*, 766–776.

Huang, C., Zhang, Z., Xu, M., Li, Y., Li, Z., Ma, Y., Cai, T., and Zhu, B. (2013). H3.3-H4 tetramer splitting events feature cell-type specific enhancers. PLoS Genet. *9*, e1003558.

Joe, A.W.B., Yi, L., Natarajan, A., Le Grand, F., So, L., Wang, J., Rudnicki, M.A., and Rossi, F.M.V. (2010). Muscle injury activates resident fibro/adipogenic progenitors that facilitate myogenesis. Nat. Cell Biol. *12*, 153–163.

Juillerat, A., Gronemeyer, T., Keppler, A., Gendreizig, S., Pick, H., Vogel, H., and Johnsson, K. (2003). Directed evolution of O6-alkylguanine-DNA alkyltransferase for efficient labeling of fusion proteins with small molecules in vivo. Chem. Biol. *10*, 313–317.

Katan-Khaykovich, Y., and Struhl, K. (2011). Splitting of H3-H4 tetramers at transcriptionally active genes undergoing dynamic histone exchange. Proc. Natl. Acad. Sci. USA *108*, 1296–1301.

Keppler, A., Gendreizig, S., Gronemeyer, T., Pick, H., Vogel, H., and Johnsson, K. (2003). A general method for the covalent labeling of fusion proteins with small molecules in vivo. Nat. Biotechnol. *21*, 86–89.

Keppler, A., Kindermann, M., Gendreizig, S., Pick, H., Vogel, H., and Johnsson, K. (2004). Labeling of fusion proteins of O6-alkylguanine-DNA alkyltransferase with small molecules in vivo and in vitro. Methods *32*, 437–444.

Kim, Y.H., Larsen, H.L., Rué, P., Lemaire, L.A., Ferrer, J., and Grapin-Botton, A. (2015). Cell cycle-dependent differentiation dynamics balances growth and endocrine differentiation in the pancreas. PLoS Biol. *13*, e1002111.

Kimura, H., and Cook, P.R. (2001). Kinetics of core histones in living human cells: little exchange of H3 and H4 and some rapid exchange of H2B. J. Cell Biol. *153*, 1341–1353.

Knoblich, J.A. (2008). Mechanisms of asymmetric stem cell division. Cell *132*, 583–597.

Kohl, J., Ng, J., Cachero, S., Ciabatti, E., Dolan, M.-J., Sutcliffe, B., Tozer, A., Ruehle, S., Krueger, D., Frechter, S., et al. (2014). Ultrafast tissue staining with chemical tags. Proc. Natl. Acad. Sci. USA *111*, E3805–E3814.

Kuang, S., Kuroda, K., Le Grand, F., and Rudnicki, M.A. (2007). Asymmetric self-renewal and commitment of satellite stem cells in muscle. Cell *129*, 999–1010.

Lahmann, I., Bröhl, D., Zyrianova, T., Isomura, A., Czajkowski, M.T., Kapoor, V., Griger, J., Ruffault, P.L., Mademtzoglou, D., Zammit, P.S., et al. (2019). Oscillations of MyoD and Hes1 proteins regulate the maintenance of activated muscle stem cells. Genes Dev. *33*, 524–535.

Lansdorp, P.M. (2007). Immortal strands? Give me a break. Cell *129*, 1244–1247.

Le Grand, F., Jones, A.E., Seale, V., Scimè, A., and Rudnicki, M.A. (2009). Wnt7a activates the planar cell polarity pathway to drive the symmetric expansion of satellite stem cells. Cell Stem Cell *4*, 535–547.

Liu, W., Wen, Y., Bi, P., Lai, X., Liu, X.S., Liu, X., and Kuang, S. (2012). Hypoxia promotes satellite cell self-renewal and enhances the efficiency of myoblast transplantation. Development *139*, 2857–2865.

Liu, J., Vidi, P.-A., Lelièvre, S.A., and Irudayaraj, J.M.K. (2015). Nanoscale histone localization in live cells reveals reduced chromatin mobility in response to DNA damage. J. Cell Sci. *128*, 599–604.

Livak, K.J., and Schmittgen, T.D. (2001). Analysis of relative gene expression data using real-time quantitative PCR and the 2(-Δ Δ C(T)) Method. Methods *25*, 402–408.

Lukjanenko, L., Jung, M.J., Hegde, N., Perruisseau-Carrier, C., Migliavacca, E., Rozo, M., Karaz, S., Jacot, G., Schmidt, M., Li, L., et al. (2016). Loss of fibronectin from the aged stem cell niche affects the regenerative capacity of skeletal muscle in mice. Nat. Med. *22*, 897–905.

Mathew, S.J., Hansen, J.M., Merrell, A.J., Murphy, M.M., Lawson, J.A., Hutcheson, D.A., Hansen, M.S., Angus-Hill, M., and Kardon, G. (2011). Connective tissue fibroblasts and Tcf4 regulate myogenesis. Development *138*, 371–384.

Mito, Y., Henikoff, J.G., and Henikoff, S. (2005). Genome-scale profiling of histone H3.3 replacement patterns. Nat. Genet. *37*, 1090–1097.

Morrison, S.J., and Kimble, J. (2006). Asymmetric and symmetric stem-cell divisions in development and cancer. Nature *441*, 1068–1074.

Muzumdar, M.D., Tasic, B., Miyamichi, K., Li, L., and Luo, L. (2007). A global double-fluorescent Cre reporter mouse. Genesis *45*, 593–605.

Nakano, S., Stillman, B., and Horvitz, H.R. (2011). Replication-coupled chromatin assembly generates a neuronal bilateral asymmetry in C. elegans. Cell *147*, 1525–1536.

Noctor, S.C., Martínez-Cerdeño, V., Ivic, L., and Kriegstein, A.R. (2004). Cortical neurons arise in symmetric and asymmetric division zones and migrate through specific phases. Nat. Neurosci. *7*, 136–144.

Pawlikowski, B., Dalla Betta, N., Antwine, T., and Olwin, B.B. (2019). Skeletal muscle stem cell self-renewal and differentiation kinetics revealed by EdU lineage tracing during regeneration. bioRxiv. https://doi.org/10.1101/627851.

Ray-Gallet, D., Woolfe, A., Vassias, I., Pellentz, C., Lacoste, N., Puri, A., Schultz, D.C., Pchelintsev, N.A., Adams, P.D., Jansen, L.E.T., and Almouzni, G. (2011). Dynamics of histone H3 deposition in vivo reveal a nucleosome gap-filling mechanism for H3.3 to maintain chromatin integrity. Mol. Cell *44*, 928–941.

Rocheteau, P., Gayraud-Morel, B., Siegl-Cachedenier, I., Blasco, M.A., and Tajbakhsh, S. (2012). A subpopulation of adult skeletal muscle stem cells retains all template DNA strands after cell division. Cell *148*, 112–125.

Rumbaugh, G., and Miller, C.A. (2011). Epigenetic changes in the brain: measuring global histone modifications. Methods Mol. Biol. *670*, 263–274.

Sambasivan, R., Gayraud-Morel, B., Dumas, G., Cimper, C., Paisant, S., Kelly, R.G., Tajbakhsh, S., and Tajbakhsh, S. (2009). Distinct regulatory cascades govern extraocular and pharyngeal arch muscle progenitor cell fates. Dev. Cell *16*, 810–821.

Simons, B.D., and Clevers, H. (2011). Strategies for homeostatic stem cell self-renewal in adult tissues. Cell *145*, 851–862.

Siwek, W., Gómez-Rodríguez, M., Sobral, D., Corrêa, I.R., Jr., and Jansen, L.E.T. (2018). time-ChIP: A Method to Determine Long-Term Locus- Specific Nucleosome Inheritance. Methods Mol. Biol. *1832*, 131–158.

Tajbakhsh, S., and Gonzalez, C. (2009). Biased segregation of DNA and centrosomes: moving together or drifting apart? Nat. Rev. Mol. Cell Biol. *10*, 804–810.

Théry, M., Racine, V., Pépin, A., Piel, M., Chen, Y., Sibarita, J.-B., and Bornens, M. (2005). The extracellular matrix guides the orientation of the cell division axis. Nat. Cell Biol. *7*, 947–953.

Tinevez, J.-Y., Perry, N., Schindelin, J., Hoopes, G.M., Reynolds, G.D., Laplantine, E., Bednarek, S.Y., Shorte, S.L., and Eliceiri, K.W. (2017). TrackMate: An open and extensible platform for single-particle tracking. Methods *115*, 80–90.

Tran, V., Lim, C., Xie, J., and Chen, X. (2012). Asymmetric division of Drosophila male germline stem cell shows asymmetric histone distribution. Science *338*, 679–682.

Troy, A., Cadwallader, A.B., Fedorov, Y., Tyner, K., Tanaka, K.K., and Olwin, B.B. (2012). Coordination of satellite cell activation and self-renewal by Par-complex-dependent asymmetric activation of p38α/β MAPK. Cell Stem Cell *11*, 541–553.

Urciuolo, A., Quarta, M., Morbidoni, V., Gattazzo, F., Molon, S., Grumati, P., Montemurro, F., Tedesco, F.S., Blaauw, B., Cossu, G., et al. (2013). Collagen VI regulates satellite cell self-renewal and muscle regeneration. Nat. Commun. *4*, 1964.

Venkei, Z.G., and Yamashita, Y.M. (2018). Emerging mechanisms of asymmetric stem cell division. J. Cell Biol. *217*, 3785–3795.

Vignaud, T., Ennomani, H., and Théry, M. (2014). Polyacrylamide hydrogel micropatterning. Methods Cell Biol. *120*, 93–116.

Voog, J., and Jones, D.L. (2010). Stem cells and the niche: a dynamic duo. Cell Stem Cell *6*, 103–115.

Webster, M.T., Manor, U., Lippincott-Schwartz, J., and Fan, C.M. (2016). Intravital Imaging Reveals Ghost Fibers as Architectural Units Guiding Myogenic Progenitors during Regeneration. Cell Stem Cell *18*, 243–252.

Wooten, M., Snedeker, J., Nizami, Z.F., Yang, X., Ranjan, R., Urban, E., Kim, J.M., Gall, J., Xiao, J., and Chen, X. (2019). Asymmetric histone inheritance via strand-specific incorporation and biased replication fork movement. Nat. Struct. Mol. Biol. *26*, 732–743.

Xie, J., Wooten, M., Tran, V., Chen, B.C., Pozmanter, C., Simbolon, C., Betzig, E., Chen, X., Tran, V., Chen, B., et al. (2015). Histone H3 threonine phosphorylation regulates asymmetric histone inheritance in the Drosophila male germline. Cell *163*, 920–933.

Xu, M., Long, C., Chen, X., Huang, C., Chen, S., and Zhu, B. (2010). Partitioning of histone H3-H4 tetramers during DNA replication-dependent chromatin assembly. Science *328*, 94–98.

Yadav, T., Quivy, J.-P., and Almouzni, G. (2018). Chromatin plasticity: A versatile landscape that underlies cell fate and identity. Science *361*, 1332–1336.

Yang, G., de Castro Reis, F., Sundukova, M., Pimpinella, S., Asaro, A., Castaldi, L., Batti, L., Bilbao, D., Reymond, L., Johnsson, K., and Heppenstall, P.A. (2015). Genetic targeting of chemical indicators in vivo. Nat. Methods *12*, 137–139.

Yennek, S., Burute, M., Théry, M., and Tajbakhsh, S. (2014). Cell adhesion geometry regulates non-random DNA segregation and asymmetric cell fates in mouse skeletal muscle stem cells. Cell Rep. *7*, 961–970.

Zhang, P., Wong, C., Liu, D., Finegold, M., Harper, J.W., and Elledge, S.J. (1999). p21(CIP1) and p57(KIP2) control muscle differentiation at the myogenin step. Genes Dev. *13*, 213–224.

STAR★METHODS

KEY RESOURCES TABLE

REAGENT or RESOURCE	SOURCE	IDENTIFIER
Antibodies		
Mouse monoclonal anti-Pax7	DSHB	Cat# PAX7; RRID: AB_2299243
Chicken polyclonal anti-GFP	Abcam	Cat# ab13970; RRID: AB_300798
Rabbit monoclonal anti-Phospho-Histone H3 (Thr3)	Millipore	Cat# 05-746R; RRID: AB_10863137
Mouse monoclonal anti-MyoD-DyLight 405	BD Biosciences / This paper	Cat# 554130; RRID: AB_395255
Mouse monoclonal anti-MyoD-DyLight 550	BD Biosciences / This paper	Cat# 554130; RRID: AB_395255
Mouse monoclonal anti-F5D	DSHB	Cat# F5D; RRID: AB_2146602
Mouse monoclonal anti-5FD-Alexa Fluor 488	DSHB / This paper	Cat# F5D; RRID: AB_2146602
Rabbit monoclonal anti-H3.3	Abnova	Cat# H00003021-K
Mouse monoclonal anti-H3.1	Johan van der Vlag	N/A
Streptavidin-Alexa Fluor 405	ThermoFisher	Cat# S32351
Donkey polyclonal anti-Chicken Alexa Fluor 594	Jackson ImmunoResearch	Cat# 703-586-155; RRID: AB_2340378
Goat polyclonal anti-Mouse IgG HRP	ThermoFisher	Cat# 31430; RRID: AB_228307
Goat polyclonal anti-Rabbit IgG HRP	ThermoFisher	Cat# 31460; RRID: AB_228341
CD31-PE Cy7	eBioscience	Cat# 25-0311-82; RRID: AB_2716949
CD45-PE Cy7	eBioscience	Cat# 25-0451-82; RRID: AB_2734986
Sca1-PE Cy7	eBioscience	Cat# 25-5981-82; RRID: AB_469669
VCam1-PE	eBioscience	Cat# 12-1061-80; RRID: AB_2572572
Chemicals, Peptides, and Recombinant Proteins		
DMEM GlutaMAX	ThermoFisher	Cat# 31966
Fetal Bovine Serum	ThermoFisher	Cat# 10270
Matrigel	Corning	Cat# 354248
MCDB	Sigma	Cat# M6770
Ultroser	Pall	Cat# 15950-017
SNAP Cell Block	New England Biolabs	Cat# S9106S
SNAP Cell TMR Star	New England Biolabs	Cat# S9105S
5-ethynyl-2′-deoxyuridine (EdU)	ThermoFisher	Cat# E10187
SNAP Cell SiR 647	New England Biolabs	Cat# S9102S
Notexin	Latoxan	Cat# L8104
Tamoxifen	Sigma	Cat# T5648
Collagenase D	Sigma	Cat# 11088882001
Trypsin	ThermoFisher	Cat# 15090
Collagenase A	Roche	Cat# 11088793001
Dispase II	Roche	Cat# 04942078001
DNase I	Sigma	Cat# 11284932
Percoll PLUS	Sigma	Cat# 17-5445-02
Poly-L-lysine polyethylene glycol	SuSoS	Cat# PLL(20)-g[3.5]-PEG(2)
Fibronectin	Sigma	Cat# F1141
Fibrinogen Alexa Fluor 488	ThermoFisher	Cat# F13191
Bind-silane	Sigma	Cat# 17-1331-01
Acrylamide	Sigma	Cat# A4058
Bis-acrylamide	Sigma	Cat# M1533
TEMED	Sigma	Cat# T9281
APS	Sigma	Cat# A3678

(*Continued on next page*)

Continued

REAGENT or RESOURCE	SOURCE	IDENTIFIER
Silicone	Smooth-on	Cat# MoldStar 20T
Hoechst 33342	ThermoFisher	Cat# H1399
Tissue Freezing Medium	Leica	Cat# 14020108926
Protein G Sepharose	Sigma	Cat# 17-0618-01
Alexa Fluor 488 NHS ester	ThermoFisher	Cat# A20000
DyLight 405 NHS ester	ThermoFisher	Cat# 46401
DyLight 550 NHS ester	ThermoFisher	Cat# 62262
Critical Commercial Assays		
Phusion Taq polymerase	New England Biolabs	Cat# M0530S
SuperScript III Reverse Transcriptase	ThermoFisher	Cat# 18080044
Ambion DNaseI	ThermoFisher	Cat# AM2222
SYBR green master mix	Roche	Cat# 04913914001
Pierce BCA Protein Assay Kit	ThermoFisher	Cat# 23227
Pierce ECL Plus Western Blotting Substrate	ThermoFisher	Cat# 32132
Click-iT Plus Alexa Fluor 488 Imaging Kit	ThermoFisher	Cat# C10637
M.O.M. Mouse Ig Blocking Reagent	Vector Laboratories	Cat# BMK-2202
M.O.M. Diluent	Vector Laboratories	Cat# BMK-2202
M.O.M. Biotinylated Anti-Mouse IgG Reagent	Vector Laboratories	Cat# BMK-2202
Deposited Data		
Experimental Models: Cell Lines		
H3.1-SNAP primary embryonic fibroblasts	This paper	N/A
H3.3-SNAP primary embryonic fibroblasts	This paper	N/A
Experimental Models: Organisms/Strains		
Mouse *Tg:H3.1-SNAP*	This paper	N/A
Mouse *Tg:H3.3-SNAP*	This paper	N/A
Mouse *Tg:Pax7-nGFP*	(Sambasivan et al., 2009)	MGI:5308730
Mouse $Pax7^{CreERT2}$	(Mathew et al., 2011)	MGI:5141477
Mouse $R26^{mTmG}$	(Muzumdar et al., 2007)	MGI:3716464
Mouse B6D2F1J	Janvier Labs	Cat# B6D2F1/JRj
Oligonucleotides		
Table S2	This paper	N/A
Recombinant DNA		
pSNAPm	New England Biolabs	Cat# N9183S
pGEM-T easy	Promega	Cat# A1360
pCAG SV40 Puro	This paper	N/A
Software and Algorithms		
Trackmate	(Tinevez et al., 2017)	N/A
Imaris 7.2.1	Bitplane	N/A
Other		
Slide-A-Lyzer MINI Dialysis Device, 10K MWCO, 2 mL	ThermoFisher	Cat# 88404
Amicon Ultra centrifugal filters	Merck	Cat# UFC801008
Slide-A-Lyzer MINI Dialysis Device, 10K MWCO, 0.1 mL	ThermoFisher	Cat# 69570
Pierce Dye Removal Columns	ThermoFisher	Cat# 22858

LEAD CONTACT AND MATERIALS AVAILABILITY

All unique/stable reagents generated in this study are available from the Lead Contact (shahragim.tajbakhsh@pasteur.fr) with a completed Materials Transfer Agreement.

EXPERIMENTAL MODEL AND SUBJECT DETAILS

Mouse strains

Tg:Pax7-nGFP (Sambasivan et al., 2009), *Pax7^{CreERT2}* (Mathew et al., 2011) and *R26^{mTmG}* (Muzumdar et al., 2007) mouse breeding was performed on an F1:C57BL6/DBA2 background. 6-8 weeks-old male littermates were used in this study, heterozygous for each allele used. Animals were handled according to national and European community guidelines, and protocols were approved by the ethics committee at Institut Pasteur.

Cell lines and culture conditions

Primary fibroblasts were derived at E13.5 and cultured in DMEM GlutaMAX (ThermoFisher) 10% Fetal Bovine Serum (FBS) 1% Penicillin-Streptomycin (PS, ThermoFisher) at 37°C 5% CO_2 3% O_2. MuSCs were plated on glass coverslips or tissue culture dishes coated with Matrigel (Corning) for 30 min at 37°C or on micropatterns in MuSC medium (40% DMEM 40% MCDB (Sigma) 20% FBS 2% Ultroser (Pall) 1% PS) at 37°C 5% CO_2 3% O_2.

METHOD DETAILS

Establishment of H3.1/H3.3-SNAP mouse strains

SNAP-tags have been used extensively to measure histone H3 variants dynamics on bulk chromatin (Adam et al., 2013; Bodor et al., 2013; Clément et al., 2018; Ray-Gallet et al., 2011), and were adapted recently to measure specific histone variants turnover genome-wide (Deaton et al., 2016). SNAP-tags react specifically and irreversibly with benzylguanine derivatives (Keppler et al., 2003). A number of cell-permeable SNAP substrates are available (fluorescent, photo-controllable, biotinylated or amenable to custom-probe synthesis through benzylguanine building blocks), with low toxicity and allowing fast and quantitative labeling (Hinner and Johnsson, 2010). SNAP-tags were reported to work efficiently and specifically *in vivo* in mice (Yang et al., 2015), and proved to be superior to classical fluorescent proteins in terms of spectral flexibility, signal-to-noise fluorescence and resistance to histological sample preparations (Kohl et al., 2014; Yang et al., 2015). Further, SNAP-tags allow the development of functionalities via synthetic substrates that cannot be achieved with classical genetically encoded reporters (Keppler et al., 2004).

Mouse H3.1 (resp. H3.3) coding sequence was PCR amplified (Phusion Taq polymerase, New England Biolabs) from mouse primary fibroblasts cDNA (SuperScript III Reverse Transcriptase, ThermoFisher) with NotI_mH3.1_F (resp. NotI_mH3.3_F) and DPPVAT_mH3.1_R (resp. DPPVAT_mH3.3_R) primers, PCR-fused to a SNAP-tag amplified from pSNAPm (New England Biolabs) with DPPVAT_SNAP_F and BamHI_SNAP_R primers, and cloned in pGEM-T easy (Promega) with T4 DNA ligase (New England Biolabs). A DPPVAT linker was included between histone coding sequences and the SNAP-tag as in Adam et al. (2013) and Ray-Gallet et al. (2011). H3.1-SNAP (resp. H3.3-SNAP) EcoRI/BamHI (New England Biolabs) fragment was subcloned in a pCAG SV40 Puro plasmid between the EcoRI and BamHI sites downstream the CAG promoter and upstream an SV40 early polyA termination sequence. CAGG H3.1/H3.3-SNAP polyA SpeI/KpnI (New England Biolabs) DNA fragments were microinjected in fertilized oocytes to derive transgenic lines.

Genotyping was performed by PCR from ear punch biopsies with CAG_For and DPPVAT_mH3.1_R or DPPVAT_mH3.R_R primers. *H3.1-SNAP* transgene insertion was mapped to chromosome 7 by inverse PCR (gDNA digestion with SacI (New England Biolabs), intramolecular ligation with T4 DNA ligase, PCR amplification with SV40 PolyA_F and SNAP qPCR_R primers). *H3.3-SNAP* transgene insertion was mapped to chromosome 10 by inverse PCR (gDNA digestion with BamHI, intramolecular ligation with T4 DNA ligase, PCR amplification with SNAP qPCR_F and CAG_R3 primers). Primers used are listed in Table S1.

qRT-PCR

Organs were homogenized in TRIzol (ThermoFisher) and RNA extracted following manufacturer's instructions. gDNA was eliminated with Ambion DNaseI (ThermoFisher) and reverse transcription performed with SuperScript III Reverse Transcriptase (ThermoFisher). RNA was eliminated with RNaseH endonuclease (Roche) for 20 min at 37°C. mRNAs level was assessed with SYBR green master mix (Roche) and analysis was performed using the $2^{-\Delta Ct}$ method (Livak and Schmittgen, 2001). RT-qPCR analyses have been normalized with *Tbp*. Specific forward and reverse primers used for qRT-PCR are listed in Table S1.

Western blot

Histones were extracted following Rumbaugh and Miller (2011) and protein concentration measured with the Pierce BCA Protein Assay Kit (ThermoFisher). 1 μg of histones was run on 4%–12% Bis-Tris Gel NuPAGE (ThermoFisher) in NuPAGE MES SDS Running Buffer (ThermoFisher) and transferred on a nitrocellulose membrane (Hybond ECL, Sigma) in 1X Tris-Glycine-SDS buffer (Euromedex) with 20% ethanol. Equivalent loading was evaluated from Ponceau staining of the membrane. The membrane was then blocked with 5% non-fat milk in Tris Buffer Saline (TBS) Tween 0.05% (TBS-T) for 20 min at RT and probed with specific primary antibodies overnight at 4°C in TBS-T 5% milk. After three washes in TBS-T, the membrane was incubated with HRP-conjugated secondary antibodies in TBS-T for 30 min at RT, washed three times in TBS-T, and revealed by chemiluminescence (Pierce ECL Plus Western Blotting Substrate, ThermoFisher) with autoradiography films (Hyperfilm ECL, GE Healthcare).

SNAP labeling

In vitro SNAP quenching (Figure 1C) was performed with 10 μM SNAP Cell Block (New England Biolabs, S9106S) for 30 min at 37°C, followed by three washes with culture medium. *In vitro* SNAP labeling was performed with 3 μM SNAP Cell TMR Star (Figure 1, New England Biolabs, S9105S) or 3 μM SNAP Cell SiR 647 (Figures 3 and 4, New England Biolabs, S9102S) in culture medium for 20 min at 37°C, followed by three washes with culture medium, and washed in culture medium for 30 min at 37°C. Sites of DNA replication were labeled with 1 μM EdU (ThermoFisher) for 10 min at 37°C. Soluble histones were extracted with CSK buffer prior to fixation as in Ray-Gallet et al. (2011). EdU incorporation was detected with the Click-iT Plus Alexa Fluor 488 Imaging Kit (ThermoFisher) as recommended.

Ex vivo SNAP labeling (Figure S3) was performed by incubating dissected and minced TA muscles in 1 mL MuSC medium containing 3 μM SNAP Cell SiR 647 for 30 min at 37°C with gentle agitation. Muscles were centrifuged at 500 g for 5 min, supernatant was discarded and muscles resuspended in 1 mL DMEM. Muscles were centrifuged at 500 g for 5 min, supernatant was discarded and muscles resuspended in collagenase D/trypsin mix for MuSC isolation (see below).

In vivo SNAP labeling was performed by injecting 10 μl of 30 μM SNAP Cell SiR 647 in NaCl 0.9% per TA at 2 or 4 dpi under isofluorane anesthesia, 8 h before tamoxifen administration (Figures 1, 2, and S1).

Muscle injury, tamoxifen and EdU delivery

Muscle injury was done as described previously (Gayraud-Morel et al., 2007). Briefly, mice were anesthetized with 0.5% Imalgene/2% Rompun. The TA muscle was injected with 15 μl of 10 μM notexin (Latoxan) in NaCl 0.9%.

Tamoxifen (Sigma) was reconstituted at 25 mg/ml in corn oil/ethanol (5%) and stored at −20°C. Before use, tamoxifen was diluted at appropriate concentration (1 mg/ml or 0.25 mg/ml) with corn oil, and administered (8 μl per g of mouse) by intragastric injection at 2 or 4 days post-injury and 14 h prior to sacrifice to allow for a maximum of two consecutive cell divisions *in vivo* (*in vivo* MuSCs doubling time about 8 h; Rocheteau et al., 2012). We optimized conditions for clonal tracing leading to two-cell clones shortly after (14 h) tamoxifen administration. Clones were defined when mGFP-labeled cells were in close proximity (< 150 μm apart, Figure S2) and isolated from any other mGFP-labeled cell. In addition, the definition of criteria for clonality was based on an extremely low dose of tamoxifen (2 μg/g of mouse, recombination frequency < 0.5%). We then used a tamoxifen dose (8 μg/g of mouse) inducing a recombination frequency about 10% to increase the sampling of the myogenic population. For each mouse, one TA muscle was used for immunohistochemistry analysis, and the contralateral TA was used for determining the recombination efficiency following dissociation and immunostaining (∼5 to 15%). EdU (ThermoFisher) was dissolved in NaCl 0.9% and injected intraperitoneally (0.3 μg/g of mouse) 9 and 7 h before tamoxifen administration.

MuSCs isolation

Dissections were done essentially as described previously (Gayraud-Morel et al., 2007). Muscles were removed from the bone in cold DMEM, minced with scissors and further digested. Injured TA muscles were digested with a mixture of 0.08% Collagenase D (Sigma), 0.1% Trypsin (ThermoFisher), 10 μg/ml DNase I (Sigma) in DMEM for five consecutive cycles of 30 min at 37°C at 60 rpm in a shaking water bath. For each round, the supernatant was filtered through a 70 μm cell strainer (Miltenyi) and collagenase and trypsin were blocked with 8% FBS on ice. Pooled supernatants from each digestion cycle were centrifuged at 500 g for 15 min at 4°C. The pellet was resuspended in 2 mL cold PBS (ThermoFisher) and placed on top of cold Percoll layers (Sigma)(5 mL of 20% Percoll and 3 mL of 60% Percoll). After centrifugation at 500 g for 15 min at 4°C, cells were collected from the 20%–60% interphase, while dense debris were concentrated below the 60% layer. The collected fraction was diluted in 40 mL DMEM 8% FBS and centrifuged at 500 g for 15 min at 4°C. The pellet was resuspended in 500 μl MuSC medium and filtered through a 40 μm cell strainer (Falcon). Cells were plated on glass coverslips coated with Matrigel or sorted using a FACS Aria III (BD Biosciences), collected in 250 μl of cold MuSC medium and plated on micropatterns (see below).

Resting hindlimb muscles (Figures 3 and 4) were digested with a mixture of 2.4U/ml Dispase II (Roche), 100 μg/ml Collagenase A (Roche) and 10 μg/ml DNase I (Roche) in Hank's Balanced Salt Solution (HBSS, GIBCO) at 37°C at 60 rpm in a shaking water bath for 90 min. The muscle suspension was then spun at 50 g for 5 min at 4°C to remove large tissue fragments. The supernatant was successively filtered through 100 μm and 70 μm cell strainers and spun at 500 g for 15 min at 4°C. The cell pellet was resuspended in HBSS 2%FBS and stained with antibodies (Sca1-PE-Cy7, CD45-PE-Cy7, CD31-PE-Cy7 and VCam1-PE) for 30 min on ice. Cells were washed twice in HBSS 2% FBS, resuspended in HBSS 2% FBS, filtered through a 40 μm cell strainer (Falcon), sorted using a FACS Aria III (BD Biosciences) and collected in cold MuSC medium. MuSCs were gated as $Sca1^-$ $CD45^-$ $CD31^-$ $VCam1^+$, according to unstained controls and single stained controls. The gating strategy yielded >95% purity in myogenic cells according to *Tg:Pax7-nGFP* controls.

Ex vivo modes of cell division

Quiescent MuSCs were isolated from hindlimb muscles of adult *Tg:H3.1-SNAP* and *Tg:H3.3-SNAP* mice by FACS with surface markers and plated on tissue culture dishes at 5000 cells/cm^2 in MuSC medium. Four days post-plating, the conditioned medium was collected and filtered, and parental histones were labeled with SNAP Cell SiR 647. Due to the variegated expression of the H3.3-SNAP reporter, H3.3-SNAP and H3.1-SNAP positive cells were enriched by FACS, plated on micropatterns in their conditioned medium and monitored by videomicroscopy for 24 h.

Micropatterns

Micropatterns were manufactured essentially as described (Vignaud et al., 2014; Yennek et al., 2014). Briefly, glass coverslips (24 × 60 mm #1, Thermo Scientific Menzel) were cleaned serially in H_2O/acetone/isopropanol, activated with an oxygen plasma treatment (Harrick Plasma) for 5 min at 30W and incubated with poly-L-lysine polyethylene glycol (PLL(20)-g[3.5]-PEG(2), SuSoS) at 100 μg/ml in 10 mM HEPES pH 7.4 at room temperature (RT) for 30 min, washed twice with H_2O and stored dried at 4°C. PLL-PEG-coated slides were placed in contact with an optical mask containing transparent micropatterns (Toppan Photomask) using H_2O (0.6 μl/cm^2) to ensure tight contact between the mask and the coverslip and then exposed to deep UV light (Jelight). Micropatterned slides were subsequently incubated with 40 μg/ml fibronectin (Sigma) and 5 μg/ml fibrinogen Alexa Fluor 488 (ThermoFisher) in 100 mM $NaHCO_3$ pH 8.3 for 25 min at RT and rinsed three times in $NaHCO_3$, three times in H_2O and dried and transferred immediately on a 12 kPa polyacrylamide (PAA) gel on silanized glass coverslips, to match the substrate rigidity of skeletal muscles (Urciuolo et al., 2013). 81 mm^2-square glass coverslips were cut out larger coverslips (22 × 22 mm #1, Thermo Scientific Menzel), cleaned serially with H_2O/EtOH 70%/EtOH 100%, deep-UV-activated, silanized with 7.1% (vol/vol) bind-silane (Sigma) and 7.1% (vol/vol) acetic acid in EtOH 99% for 10 min at RT, washed twice with EtOH 99% and dried. Transfer of micropatterns on PAA gel was performed with 7 μl/cm^2 of a solution containing 7.5% acrylamide (Sigma), 0.16% bis-acrylamide (Sigma), 0.05% TEMED (Sigma), 0.05% APS (Sigma, A3678) in HEPES 10 mM pH 7.4 for 45 min at RT. Gels were rehydrated in $NaHCO_3$ 100 mM pH 8.3 for 15 min at RT, detached from patterned coverslips and washed with PBS three times before cell seeding.

Micropatterned PAA gels were transferred in an in-house-made glass-bottom 6 well Petri dish to allow live-imaging and PAA embedding before immunostaining (see below). Briefly, 32 mm diameter glass coverslips were cleaned and silanized, a 14 × 14 × 0.45 mm piece of silicone (Smooth-on) was put at the center, and coverslips were layered with a 12 kPa PAA gel ('surrounding' PAA). After PAA polymerization, the coverslips were sealed (silicone) to the bottom of a 6 well plate (TPP) drilled out to 30 mm diameter. The silicone at the center of the PAA gel was removed and replaced with a 16 × 16 × 3 mm silicone isolator with a 10 × 10 × 3 mm window at the center to fit micropatterned PAA gels (9 × 9 mm) after filling with PBS. The apparatus was washed several times and equilibrated with MuSC medium. Medium was removed completely and cells (250 μl) seeded within the silicone isolator on micropatterns and, 90 min after plating, nonattached cells were washed with medium and medium volume was adjusted to 5 ml.

Live-imaging

Live-imaging was performed using a Zeiss Observer.Z1 microscope connected to an LCI PlnN 10x/0.8 W DICII objective and Hamamatsu Orca Flash 4 camera piloted with Zen (Zeiss). Cells on micropatterns were filmed and images were taken every 9 min with bright-field filter to ensure that single cells were plated on the micropatterns and that their progeny remained confined. The raw data were analyzed with TrackMate (Tinevez et al., 2017).

Immunocytochemistry and Immunohistochemistry

Cells on micropatterns were fixed in 4% paraformaldehyde (PFA, Electron Microscopy Sciences) in PBS containing 0.9 mM $CaCl_2$ and 0.5 mM $MgCl_2$ (PBS Ca^{2+} Mg^{2+}) for 5 min at RT and washed in PBS Ca^{2+} Mg^{2+} for 5 min at RT. To prevent cell loss during subsequent immunostaining steps, cells were embedded in PAA. Cells were equilibrated in a solution containing 3.82% acrylamide, 0.13% bis-acrylamide and 0.1% TEMED in PBS for 30 min at RT, and the solution was replaced with 3.82% acrylamide, 0.13% bis-acrylamide, 0.1% TEMED and 0.05% APS in PBS. The silicone isolator was carefully detached and a parafilm-covered 20 × 20 mm glass coverslip (20 × 20 mm #1, Thermo Scientific Menzel) was adjusted on top of the micropatterns, sitting on the 'surrounding' PAA. Excess polymerization solution was removed and PAA allowed to polymerize for 1 h at RT. After rehydration in PBS for 15 min, the parafilm-covered coverslip was detached, PAA-embedded micropatterns were recovered and washed several times in PBS. Cells were permeabilized in 0.5% Triton X-100 (Sigma) for 20 min at RT, washed three times 10 min in PBS, blocked in 10% goat serum (GS, GIBCO) for 4 h at RT, incubated with primary antibodies overnight at 4°C in 2% GS, washed four times 1 h in PBS at 4°C, incubated with Alexa Fluor-conjugated secondary antibodies and Hoechst when required overnight at 4°C in 2% GS and washed four times 1 h in PBS at 4°C. For Pax7/Myog double staining (Figures 3 and 4) and Pax7/Myod/Myog triple staining (Figure S3), cells were further blocked with Pax7 primary antibody overnight at 4°C in 2% GS, washed four times 1 h in PBS at 4°C, incubated with Alexa Fluor 488-conjugated anti-Myogenin and/or DyLight 405-conjugated anti-Myod antibodies (see below) in 2% GS overnight at 4°C and washed four times 1 h in PBS at 4°C.

Cells on glass coverslips were fixed in 4% PFA for 5 min at RT, washed twice in PBS, permeabilized in 0.5% Triton X-100 for 5 min, blocked in 10% GS for 30 min at RT, incubated with primary antibodies in 2% GS for 2 h at RT, washed in PBS three times 5 min, incubated with Alexa Fluor-conjugated secondary antibodies and Hoechst for 45 min at RT, washed in PBS three times 5 min and mounted in PBS Glycerol 75%.

For immunohistochemistry, TA muscles were fixed for 24 h in 4% PFA at 4°C, washed in cold PBS four times 1 h at 4°C, equilibrated in 20% sucrose (Sigma) overnight at 4°C, embedded in Tissue Freezing Medium (Leica) and snap-frozen on liquid nitrogen. 12 μm cryosections were allowed to dry at RT for 30 min and rehydrated in PBS for 15 min. Antigen retrieval was performed in Tris 10 mM EDTA 1 mM pH 9 for 10 min at 95°C, followed by three short PBS washes and an additional wash in PBS for 30 min at RT. Sections were permeabilized in 0.5% Triton X-100 for 20 min at RT, washed three times in PBS, blocked in M.O.M. Mouse Ig Blocking Reagent (Vector Laboratories) for 1 h at RT, washed three times in PBS, incubated in M.O.M. Diluent (Vector Laboratories) for 5 min at RT,

incubated with primary antibodies (Pax7 (Figures 2B–2D, S1A–S1F, and S2A) or anti-Myogenin 5FD (Figures 2E–2G, S1G, and S2B), GFP, in M.O.M. Diluent) for 1 h at RT, washed three times 5 min in PBS, incubated with M.O.M. Biotinylated Anti-Mouse IgG Reagent (Vector Laboratories) for 10 min at RT, washed three times 5 min in PBS, incubated with secondary antibodies (Streptavidin-Alexa Fluor 405, Donkey anti-Chick Alexa Fluor 594, in M.O.M. Diluent) for 30 min at RT, washed three times 5 min in PBS. For Pax7/Myod/Myog triple staining, sections were further blocked with anti-Pax7 antibody (in M.O.M. Diluent) for 1 h at RT, washed three times 5 min in PBS, incubated with Alexa Fluor 488-conjugated anti-Myogenin and DyLight 550-conjugated anti-Myod antibodies (see below, in M.O.M. Diluent) overnight at 4°C, washed in PBS three times 5 min and mounted in PBS Glycerol 75%. EdU incorporation was detected with the Click-iT Plus Alexa Fluor 488 Imaging Kit (ThermoFisher) as recommended.

We readily detected SNAP signal after histological preparation (strong fixation and heat-induced epitope retrieval), while mGFP fluorescence was lost and required immunodetection, confirming superiority of synthetic SNAP fluorophores over classical fluorescent proteins. Immunostainings were analyzed with a Zeiss Observer.Z1 and a Zeiss LSM800 confocal microscopes. Images were processed with Imaris 7.2.1 software.

Antibody fluorescent labeling

Anti-Myogenin antibody (5FD, DSHB) was purified with protein G Sepharose (Sigma) as recommended. Briefly, hybridoma supernatant was incubated with protein G Sepharose overnight at 4°C and packed into polypropylene columns (QIAGEN), washed five times with PBS and antibody was eluted twice with 1.5 mL glycine 100 mM pH 2.7, neutralized with 150 µl Tris 1M pH 9. Elution fractions were pooled and dialyzed (ThermoFisher) against PBS overnight at 4°C. Antibody was concentrated with Amicon Ultra centrifugal filters (Merck) to 1 mg/ml. 100 µl of purified F5D antibody at 1 mg/ml (resp. anti-Myod at 0.75 mg/ml (BD Bioscience)) were dialysed (Thermofisher) against $NaHCO_3$ 100 mM pH 8.3 (resp. $Na_2B_4O_7$ 50 mM pH 8.5) overnight at 4°C, incubated with 120 µM Alexa Fluor 488 NHS ester (ThermoFisher)(resp. 60 µM DyLight 405 NHS ester (ThermoFisher) or 70 µM DyLight 550 NHS ester (ThermoFisher)) at 23°C for 1 h. NaCl concentration was adjusted to 150 mM and excess fluorescent dye was removed with Pierce Dye Removal Columns (ThermoFisher) following manufacturer's recommendations. Desalted labeled antibodies were further dialysed (ThermoFisher, Cat#69570) against PBS overnight at 4°C and stored at −20°C with 1 mg/ml bovine serum albumin (Sigma) and 50% glycerol.

Image analysis and quantification

For each cell within a pair (Figures 2, 3, S1, S3, and S4) or a cluster of 3 cells (Figure 4), the fluorescence intensities of transcription factors and EdU were measured on segmented nuclei and expressed as a percentage of their respective mean intensity measured over all cells of all pairs and/or clusters (*ie* all cell pairs *in vivo* at 3 dpi (Figure S1C), all cell pairs *in vivo* at 5 dpi (Figures 2B–2D and S1F; Figures 2E–2G and S1G right), all cell pairs on micropatterns from *in vivo* activated cells (Figure S3), all cell pairs and clusters of 3 cells on micropatterns from *ex vivo* activated cells (Figures 3, 4, and S4). For each cell within a pair or a cluster of 3 cells, SNAP intensity was measured on segmented nuclei and expressed as a percentage of the maximum intensity within its pair or cluster of 3 cells.

Analysis of parental histone distribution

To analyze parental histone distribution independently of modes of cell divisions or DNA segregation, cells within cell pairs or clusters of 3 cells were ranked with decreasing normalized SNAP intensity and named 'Cell X' and 'Cell Y' for cell pairs (Figures S1B, S1D right, S1E, and S1G left) and 'Cell X', 'Cell Y' and 'Cell Z' for clusters of 3 cells (Figures 4D–4G). Clusters of 3 cells were further classified according to the four different types we observed (Figure 4). Data are then presented as mean normalized fluorescence intensity of cells X, cells Y (and cells Z) ± SD of all pairs (clusters of 3 cells).

To analyze parental histone distribution according to modes of cell division or DNA segregation, cells within cell pairs were ranked with decreasing normalized Pax7 (Figures 2D, 3, S1F, and S3), Myogenin (Figure S1C) or EdU intensity (Figures 2G and S1G right) and named 'Cell A' and 'Cell B'. Data were then presented as mean normalized fluorescence intensity of cells A and cells B ± SD of all pairs.

Analysis of modes of cell division

Ex vivo modes of cell division (Figures 3, 4, S3, and S4) were determined by calculating a fold change for cell fate markers between the cells with maximum and minimum intensities for each cell pair. Modes of cell division were called symmetric if Pax7 and Myogenin were displaying fold changes < 2. SCDs were called self-renewing in case of symmetric Pax7 expression, and differentiating in case of symmetric Myogenin expression. Cell divisions were called asymmetric in case of a cell fate marker with a fold change >2.

In vivo modes of cell division (Figures 2B–2D, S1C, and S1F) were determined according to Pax7 and Myogenin expression patterns: symmetric presence of Pax7 (Figures 2B–2D and S1F) or absence of Myogenin (Figure S1C) = self-renewing SCD, symmetric absence of Pax7 (Figures 2B–2D and S1F) or presence of Myogenin (Figure S1C) = differentiating SCDs, asymmetric Pax7 and/or Myogenin expression (Figures 2B–2D, S1C, and S1F) = ACDs.

In vivo modes of DNA segregation (Figures 2E–2G and S1G right) were determined according to EdU incorporation patterns (symmetric presence = random DNA segregation, asymmetric presence = non-random DNA segregation).

Expected frequencies of clusters of 3 cells (Figure 4B top panel) were calculated based on observed frequencies of different modes of cell division (Figure 4H) and assuming that the first and second divisions follow the same ratios.

Clusters of 3 cells would arise from the division of a single cell, followed by the division of one of the resulting daughter cells. The first division would give rise to three types of cell pairs: $Pax7^+/Pax7^+$ (23.2%), $Pax7^+/Myog^+$ (40.4%) and $Myog^+/Myog^+$ (36.4%) (Figure 4H, averages from Figure 3). As $Myog^+$ cells are post-mitotic, $Myog^+/Myog^+$ cell pairs were assumed to not generate clusters of 3 cells. Hence, clusters of 3 cells were classed as derived from $Pax7^+/Pax7^+$ (36.5%) and $Pax7^+/Myog^+$ (63.5%) cell pairs.

$Pax7^+/Pax7^+$ cell pairs can generate three types of 3-cell clusters: $Pax7^+/Pax7^+/Pax7^+$ (8.5%), $Pax7^+/Pax7^+/Myog^+$ (14.7%), and $Pax7^+/Myog^+/Myog^+$ (13.3%).

$Pax7^+/Myog^+$ cell pairs can generate three types of 3-cell clusters: $Pax7^+/Pax7^+/Myog^+$ (14.7%), $Pax7^+/Myog^+/Myog^+$ (25.7%), and $Myog^+/Myog^+/Myog^+$ (23.1%).

Overall, clusters of 3 cells with the following frequencies were expected: $Pax7^+/Pax7^+/Pax7^+$ (8.5%), $Pax7^+/Pax7^+/Myog^+$ (14.7 + 14.7 = 29.4%), $Pax7^+/Myog^+/Myog^+$ (13.3 + 25.7 = 39%) and $Myog^+/Myog^+/Myog^+$ (23.1%) (Figure 4B top panel).

Frequencies of different modes of cell division at the second division *ex* vivo on micropatterns (Figure 4I) were calculated from observed frequencies of each scenario yielding each cluster of 3 cells (Figures 4D–4G). The frequency of self-renewing SCDs was calculated from frequencies observed in Figures 4D and 4E left. Frequency of differentiating SCDs was calculated from the frequencies observed in Figures 4F and 4G right. Frequency of ACDs was calculated from frequencies observed in Figures 4E right and 4G left.

QUANTIFICATION AND STATISTICAL ANALYSIS

Bar charts represent the mean ± standard error of the mean (SEM) or standard deviation of the mean (SD) as specified in figure legends. Definitions of n-values are reported in figure legends. No method was used to determine whether the data met assumptions of the statistical approach.

DATA AND CODE AVAILABILITY

This study did not generate any unique datasets or code.